2020

Characterizing Solar Cells

Katheryn R. Kornegay
Pomona College

Recommended Citation

Kornegay, Katheryn R., "Characterizing Solar Cells" (2020). *Pomona Senior Theses*. 226.
https://scholarship.claremont.edu/pomona_theses/226

Characterizing Solar Cells

A thesis submitted in partial fulfillment of the requirements of a degree of
Bachelor of Arts in
Physics
at
Pomona College

Katheryn Kornegay
with
Janice Hudgings, Ph.D.
Professor of Physics
Pomona College

February 7, 2020

Abstract

Perovskite solar cells and organic photovoltaics are both attractive because of their potential flexibility, tunable material properties, and low cost. Though perovskite solar cells have reached efficiencies comparable to conventional silicon solar cells, these have only occurred with lab-scale devices. Organic photovoltaics have much lower operating efficiencies than both perovskite and silicon solar cells, often due to non-uniformities and defects. In this thesis, we use two different techniques to better characterize these two types of solar cells. For perovskite solar cells, we use a drift-diffusion model, to characterize the transition between different doped states in its hole-transport layer, Spiro-OMeTAD, and investigate the effect on its mobility and charge-carrier density. We then compare results found from using the drift-diffusion model with other simple models. For organic photovoltaics, we use high spatially resolved thermoreflectance imaging to examine electrical shunts and other defects in PCBM-based devices under electrical. We find unexplained whole-cell heating with voltage biasing. Using our techniques used in this thesis, combined with results from other conventional techniques, will allow us to better understand, characterize and ultimately further improve performance of all solar cells.

Acknowledgements

To my NYU Tandon School of Engineering Team: Thank you to Dr. André Taylor for providing me with the opportunity to work in your lab over the summer. Thank you to Dr. Jason A. Rohr for working closely with me with the research. Your patience allowed me to better understand the research's objectives and goals. Thank you to Dr. Roderick Mackenzie for letting me use and edit your model software. Thank you to Dr. Jaemin Kong for allowing me to use your data as a starting ground and reference. Thank you to the rest of the post-docs, graduates and undergraduates in Dr. Taylor's lab this past summer. Your feedback and collaboration really allowed for a fun and thought-provoking summer. Finally, thank you to NYU's Tandon School of Engineering Junior Summer Program, for accepting me and making sure I had everything I needed to succeed this past summer.

To my Pomona College Team: Thank you to Dr. David Tannenbaum for allowing me to use his solar cell equipment and solar cells made by Sabrina Li (PO '17). Thank you to Tony Grisby, Hardy Richardson, and David Haley for helping build the mount for the solar cells and providing help and support whenever it was needed. Thank you to Fernando Ayala and Tyler Jones (PO '18) for teaching me everything about imaging organic photovoltaics with thermoreflectance, how to operate the machines necessary to complete the project and so much more. Thank you to Valerie Wang (PO '20) and Alfred Molina (PO '21) for working with me this past year trying to debug our research and for picking up the torch to this project. Thank you to the rest of Dr. Hudgings' lab for your feedback and support on this research project.

Last but not least, I would like to thank Dr. Janice Hudgings for being my research advisor over the past three years. Her guidance and mentorship have allowed me to conduct research on my interests and have taught me how to mentor other students in class and on projects. Her confidence in me has helped me preserver throughout this project and my time at Pomona.

To my friends and family: Thank you to the students in the physics department. We struggled, laughed, stressed and persevered through classes together. Thank you to my friends outside of the department. Your love and support got me through Pomona. Finally, thank you to my brother, Benjamin, and my parents Felecia and Ben Kornegay. Your love, sacrifices, and guidance have gotten me to where I am today and where I am headed. Much love and gratitude from big head.

Contents

1 Introduction

1.1 The World's Energy Sources

As the population of the world increases, the amount of energy sources needed to satisfy humans also grows. These energy sources can be broken down into three major categories: fossil fuels, nuclear energy, and renewable energy [1]. Fig. 1.1 shows the breakdown of the world's electricity production in 2017. Fossil fuels (this includes petroleum, natural gas, and coal) are the only energy sources which emit carbon dioxide (CO_2). These accounted for about 79% of U.S.'s energy consumption in 2018 and produced about 65% of the world's electricity in 2017 [2, 3]. Although fossil fuels are currently dominating throughout the world, they contribute the most to climate change. For that reason, governments and citizens are trying to shift toward prioritizing the other two major energy sources. In 2017, about 10% of the world's electricity was produced by nuclear energy from just over 440 power plants [3]. While nuclear energy does not emit (CO_2), there are still very significant environmental dangers with this source. As seen with Fukushima, Chernobyl and Three Mile Island, failed nuclear power plants are fatal to humans and the surrounding ecosystems. In addition, there has been little planning for dealing with old fuel rods, which are very toxic to the environment, used in these plants. Though there are still a few plants in the process of being built, less governments are turning to this source. The final energy source, renewable energy, only produced about 7% of the world's energy and accounted for 11% of U.S.'s energy consumption in 2017 [3, 4]. Renewable energy does not emit CO2 and has no immediate environmental danger. Renewable energy consists of hydro-power, biomass, wind, geothermal, and solar energy. Solar energy is a viable energy source because the sun is an unlimited energy source, with no negative effect on the environment. This thesis further explores properties of solar cells, a device which allows for the sun to be used as an energy source.

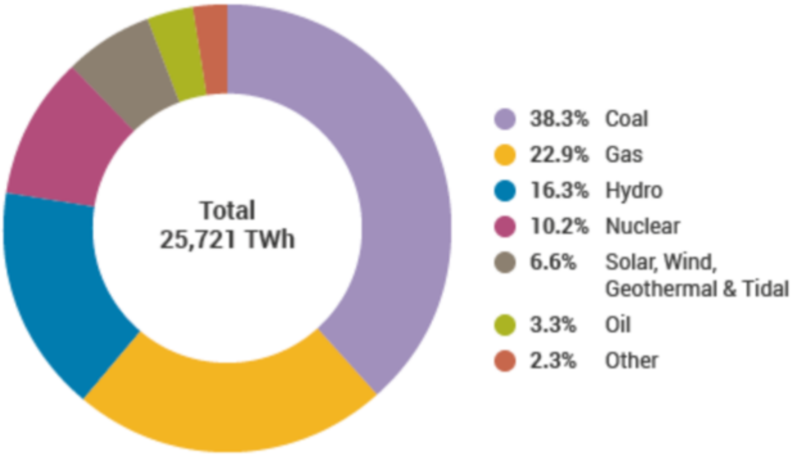

Figure 1.1: The world's electricity production broken into percentages produced by different energy sources [3].

1.2 Types of Solar Cells

The very first solar cell was created by Charles Fritts, who in 1883 used selenium on a thin gold layer, producing an overall of efficiency of less than 1% [5]. Since then, the materials used in solar cells have changed drastically, and their efficiencies have increased significantly. The biggest difference between solar cells are their active layers, or the layers where solar light is absorbed and converted into electricity. In addition to their different active layers, different types of solar cells have specific applications. For example, three-junction solar cells, around 38% efficient, are used on solar panels in space, whereas crystalline silicon solar cells, around 27% efficient, are used on solar panels of homes. Fig. 1.2 shows the development of different solar cells and their efficiencies from the mid-1970s to the mid-2010s. This thesis focuses on two emerging type of thin-film solar cells: perovskite solar cells and organic photovoltaics. Fig. 1.3 is a slice of NREL's chart highlighting these two solar cells and the most commonly commercially used silicon solar cell, together with their current efficiencies.

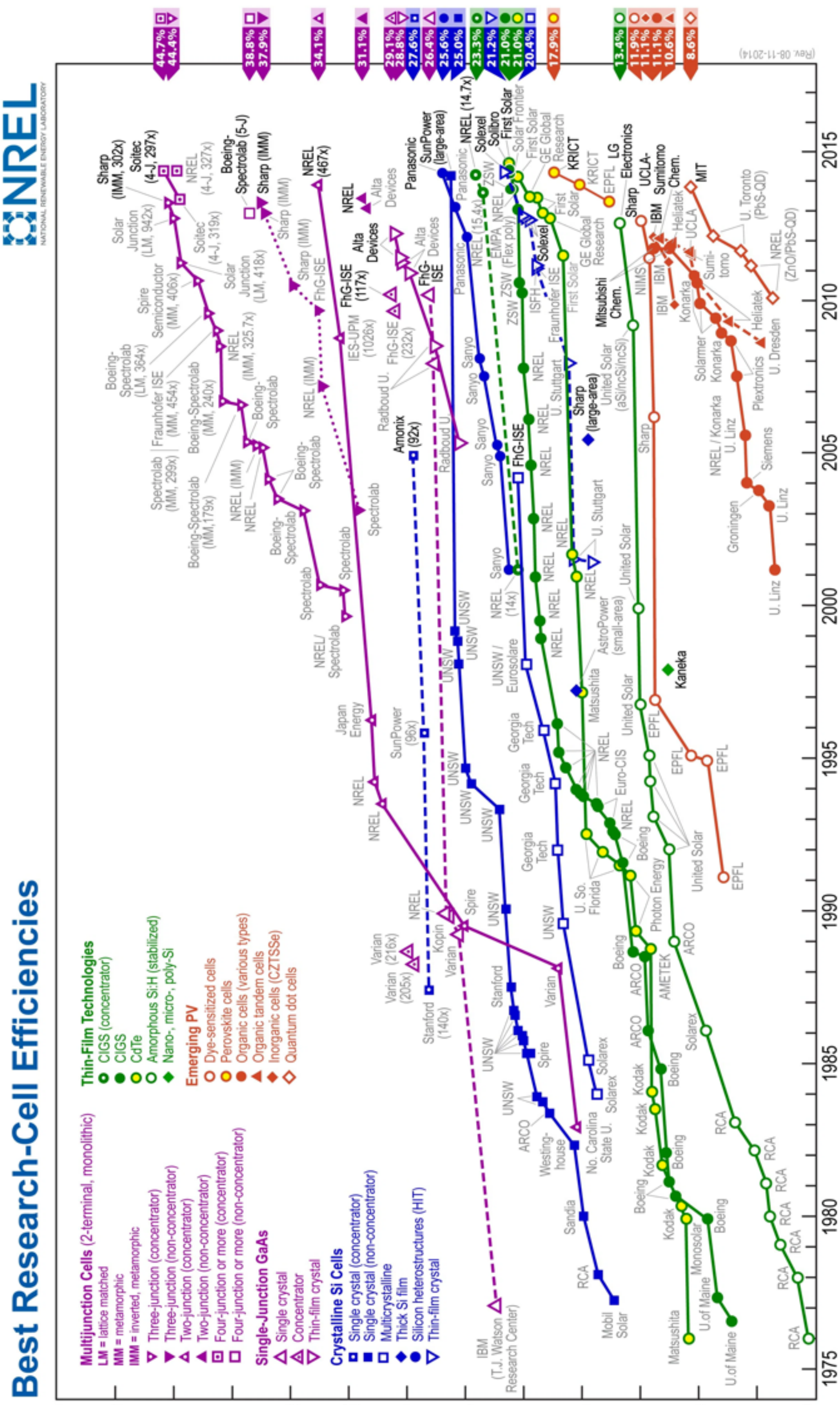

Figure 1.2: National Renewable Laboratory's report on best research-cell efficiencies for the last four decades [6].

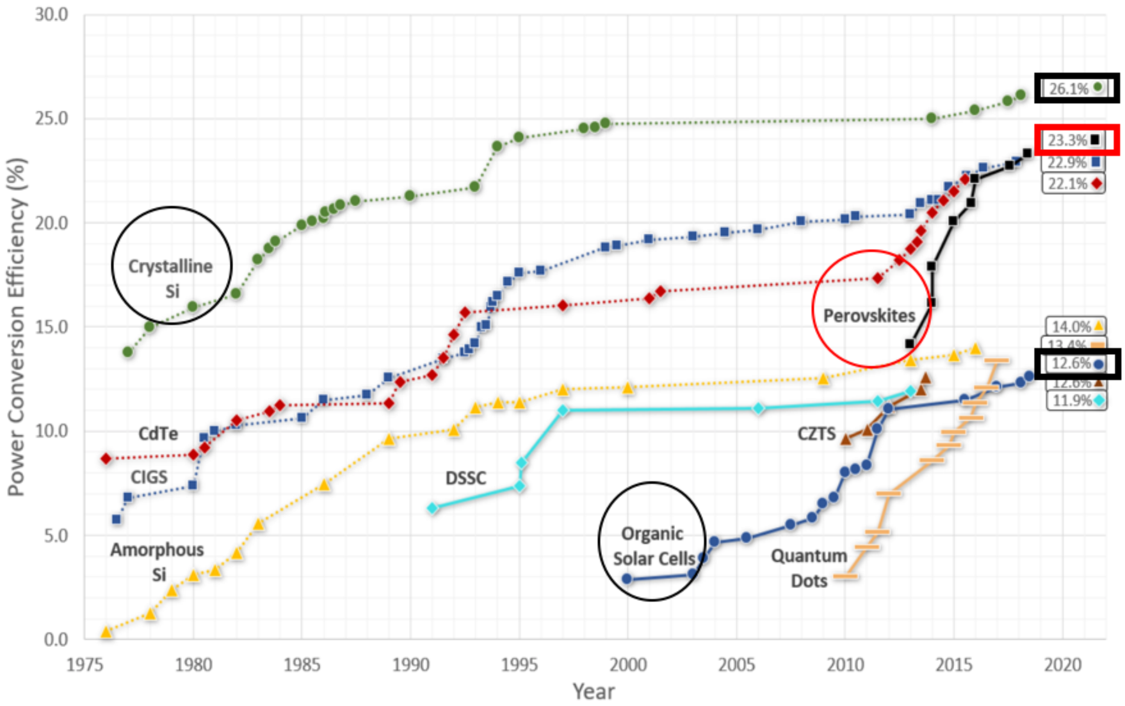

Figure 1.3: A slice of NREL's original chart, highlighting the most commercialized silicon solar cell and the two solar cells focused on in this thesis, perovskite and organic solar cells, as well as their most research efficiencies [7].

1.2.1 Silicon Solar Cells

Silicon (Si) solar cells are the most thoroughly researched cells. While the first report of a Si solar cell was in 1940, the first practical Si cell was created in 1954 by Bell Labs researchers Pearson, Chapin, and Fuller, with an efficiency of 8% [8,5]. Since then, Si solar cells, specifically crystalline, have one of the highest efficiencies of solar cells commercialized today. In 2016, about 90% of solar panels on the market were Si based [9]. These cells are able to absorb a significant amount of the sun's light. However, in order for Si solar cells to be efficient, the Si needs to be 99.999% pure and needs more than 1,000 times material in its active layer than other thin-film solar cells [9]. Though the cost of Si has decline more over the years, there is a limited amount of pure Si in the world. The next two solar cells have the potential to also be commercialized, although they are to date still mostly in research labs.

1.2.2 Perovskite Solar Cells

Perovskite solar cells (PSCs) were first discovered in 2009 by Miyasaka and his colleagues [10]. Perovskite, which refers to its crystal structure, uses a lead-based halide as the active layer in the solar cell. Since their discovery, PSCs have had an impressive growth in efficiency, from less than 4% in 2009 to over 22% in 2016 [10]. What makes perovskites intriguing are its low-cost materials used for fabrication, its ability to be solution-processed, and its mechanically flexible properties that would allow for them to be used in applications where conventional rigid silicon solar cells would not work. However, PSCs have a much shorter lifespan and device stability than other solar cells. They begin to degrade when exposed to oxygen, moisture, UV light, and heat, so PSCs would not last long in the real environment [10]. In addition to their chemical and thermal instability, PSCs are also mechanically unstable, often considered the most fragile of the solar cells [11]. Yet due to their quick growth in efficiency within the last decades, PSCs could be potential competitors to Si solar cells by the end of the next decade.

1.2.3 Organic Photovoltaics

Organic photovoltaics (OPVs) were first fabricated by Tang in 1986 [11]. Organic refers to the carbon-based polymer used as the active layer in the device. Similar to PSCs, OPVs are attractive because of their mechanical flexibility, tunable material properties, and potentially low cost [12]. Unlike PSCs, OPVs have not had as rapid of a growth in efficiency, only having recently reached 17% [12]. In addition, OPVs cannot absorb as much of the sun's light as Si solar cells or PSCs. OPVs have low-carrier mobility and begin to degrade when exposed to oxygen and moisture or if there any defects within the active layer [13]. They also struggle to maintain their efficiency and stability over a long period of time. Though, OPVs may never reach the efficiency of Si solar cells and PSCs, they still hold great potential for use in smaller applications.

1.3 Thesis Objective

There is still a significant amount of research that must be done before PSCs and OPVs can be considered market competitive. Through modeling and experimental investigation, researchers work to further improve these solar cells. In this thesis, we use two techniques to investigate the issues of

PSCs and OPVs. Chapter 3 explores a modeling technique used for PSCs. We use a drift-diffusion analytical model to confirm and understand the characteristics of hole mobility and charge carrier density in one particular layer, Spiro-OMeTAD. We aim to show that using this drift-diffusion model is more accurate in characterizing Spiro-OMeTAD than other simplified analytical models that are typically used. Chapter 4 explores an imaging technique for OPVs. We use high-spatial-resolution thermoreflectance imaging to detect and characterize defects in devices. We aim to compare our data with data from conventional imaging techniques. Ultimately, we hope to show that using different kind of techniques and investigations enables researchers to achieve a wholistic understanding of solar cells and how to improve them.

2 Theory of Solar Cells

Solar cells allow access to the world's largest and most renewable energy source, the sun, by converting sunlight into electricity. This chapter will break down how solar cells function as well as some general ways that solar cells are typically characterized.

2.1 Sunlight

The light from the sun can be modeled both as an electromagnetic wave as well as a collection of particles or photons. The sun emits certain wavelengths of light which bombard the earth, as seen in Fig. 2.1. This graph shows the photon flux density versus the wavelength of these photons when sunlight reaches the top of Earth's atmosphere and the Earth's surface. More than half of sunlight is outside of the visible spectrum. Materials within solar cells should capture as much of the sunlight's spectrum as possible in order to maximize efficiency.

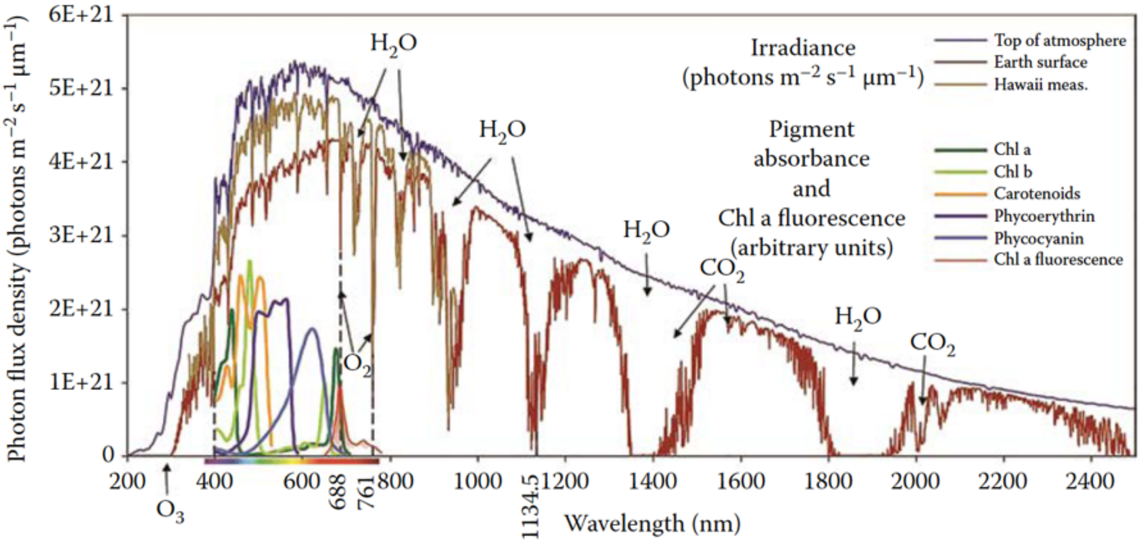

Figure 2.1: Graph of the sunlight spectrum, showing the photon flux density versus the wavelength of the photons. This looks specifically at the photons reaching the top of the atmosphere, the Earth's surface, and photons absorbed in the photosynthetic pigments in plants and algae (Chl a, Chl b, Carotenoids, Phycoerythrin, Phycocyanin, and Chl a fluorescence) [14].

2.2 Photoelectric Effect

The process of a material capturing and converting sunlight is called the photoelectric effect, shown in Fig. 2.2. A photon of a certain wavelength and energy is absorbed by a material, exciting an electron, or a charge carrier, from the valence band to the conduction band. This creates a "free-space" or a hole, also a charge carrier, left in the valence band of a material. An electron in the valence band will replace the hole with itself, again creating a hole. The movement of electrons create a current as electrons flow throughout the semiconductor attempting to fill holes. The process continues for a while, until the excited electron falls back to the valence band, also known as recombination. The best material for the photoelectric effect is a semiconductor because the energy gap, ΔE, between both bands is small enough that excited electrons can easily move between the bands, and large enough to be able to create electron-hole pairs. Semiconductors are the major factor that allows for solar cells to function properly.

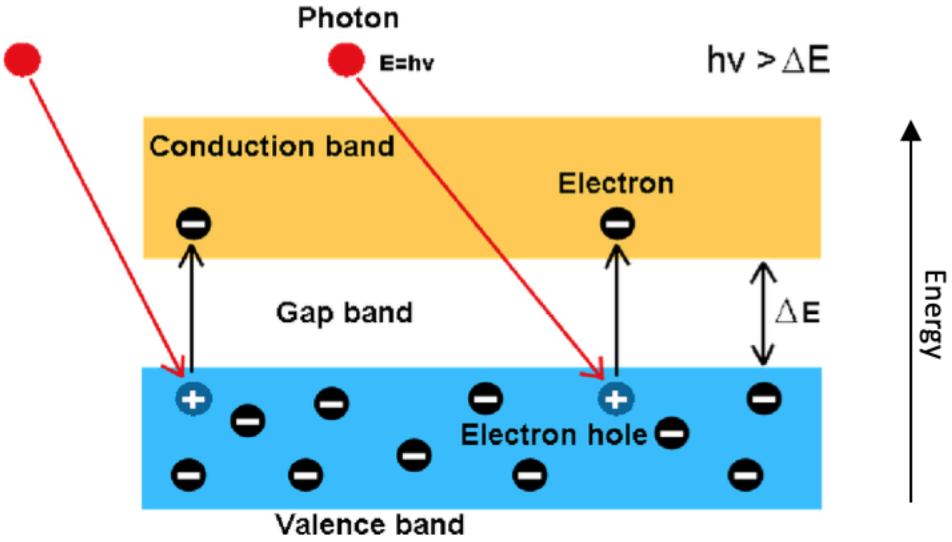

Figure 2.2: Diagram of the photoelectric effect for a semiconductor. A photon with an E equal to hν, where hν is larger than the energy gap, ΔE, of the semiconductor is absorbed in its valence band. An excited electron "jumps" to the conduction band leaving a hole, creating an electron-hole pair [15].

2.3 General Solar Cell Structure

Fig. 2.6 shows the general structure of a solar cell. Solar cells allow photons to pass through a transparent substrate, typically glass and then absorbed in the intrinsic layer. The photon causes an excited electron to move n-doped layer and the cathode or the metal, and the hole moves toward the p-doped layer and the anode or ITO (indium tin oxide). The cathode is then connected to the positive end of an external load, such as a battery, and the anode to the negative to complete the circuit. The movement of electrons and holes are what create current and electricity. While solar cells have similar make-ups, their layers differ drastically. This thesis focuses PSCs and OPVs.

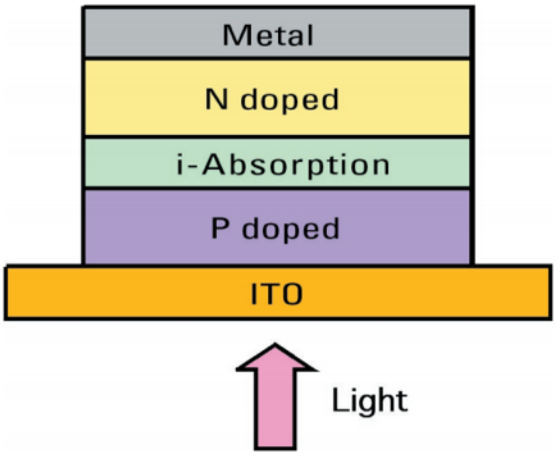

Figure 2.3: General structure of a PIN solar cell [16].

2.4 PIN Solar Cell

A semiconductor alone does not convert sunlight into electricity. A semiconductor device is an electronic device and uses the electrical properties of a semiconductor to be able to create electricity. An example of one electronic device is a diode, which allows for current to flow only one direction [17]. A diode joins a n-type or p-type semiconductor with a metal, making current flow more easily. A n-type semiconductor uses electrons as the dominant charger carrier, where a p-type semiconductor uses holes, allowing for electrical conduction. In a similar fashion to a diode, a solar cell contains an intrinsic layer (a layer neither p-type nor n-type) sandwiched by a p-doped layer with a large work function and a n-doped layer with a smaller work function, where there are more electrons than holes in the overall system when the layer is unbiased. A work function is the minimum amount of energy needed to remove an electron from the surface of a metal. The difference in work functions form the slant conduction and valence bands in Fig. 2.5 [14]. No longer are the bends of the bands due to the electrons, but due to the junction of the p-doped and n-doped layers and now there exists a built-in voltage, -qV_{bi}. This sandwich is typically called a PIN solar cell. When a voltage is applied, the slant in the bands become more horizontal, and once completely horizontal it is possible to find the open-circuit voltage (V_{OC}). Once again, the main benefit of having selecting layers is to lessen the amount of recombination of electron-holes pairs within the solar cell, with electron moving toward n-doped layer, and the holes toward the p-doped layer.

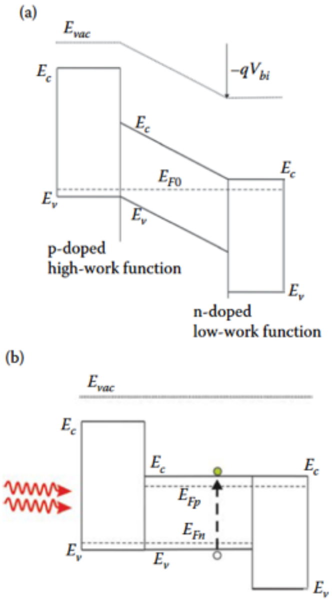

Figure 2.4: Energy diagram of what occurs to the energy levels of a PIN solar cell at a) an equilibrium state and b) in open-circuit conditions. At an equilibrium state, the energy levels, E_V, E_C, E_vac, are slanted with a built-in voltage, -qV_{bi}. When in an open-circuit condition, the levels flatten. [14].

2.5 Carrier-Selective Contacts

2.5.1 Schottky Barrier Junction

When semiconductor come into contact with a metal, they form a junction. One such junction is the Schottky barrier junction. Fig. 2.3 shows the energy diagram of a Schottky barrier junction at the contact between a metal, to the left of the rectifying contact, and a n-type semiconductor to the right [14]. When the metal and semiconductor are in contact, the energy levels of the conduction and valence band bend due to the electrons as seen in Fig. 2.3.

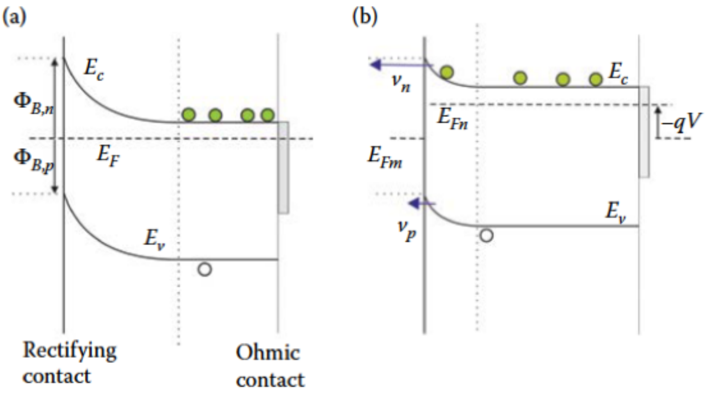

Figure 2.5: Energy diagram of a Schottky Barrier Junction at a) an equilibrium state and b) a forward bias, where the metal is to the left of the barrier (the rectifying contact) and the n-type semiconductor is to the right. $\Phi_{B,n}$ and $\Phi_{B,p}$ represent the energy level or work function at the Schottky barrier for electron and holes respectively. E_V, E_C, and E_F represent the energy for the valence, conduction and Fermi level at equilibrium (energy difference between the lowest occupied state of conduction band and highest occupied state of valence band). E_{Fn} and E_{Fm} represent the new Fermi energy level for the metal and semiconductor, respectively, when a voltage, $-qV$, is applied. v_n and v_p represent the velocity and direction of the electrons and holes respectively when $-qV$ is applied [14].

When the work function of the metal is larger than the semiconductor's, the dominant carriers in the n-type semiconductor will have a higher potential energy than those in the metal [14]. To create an equilibrium state, free electrons from the conduction band of the semiconductor will move toward the metal, creating holes, as seen in Fig. 2.3.a. For every electron moved from the semiconductor to the metal, a hole will take its place. When a battery is added to the system such that the positive terminal is connected to the metal and the negative terminal is connected to the semiconductor, the system experiences a forward bias, as seen in Fig. 2.3.b. With a steady applied voltage, the electrons flow from the semiconductor into the metal, creating a current and thus a diode device. In order for a steady current to flow the applied voltage must be above the system's built in voltage [18]. If the battery is connected with the terminals reversed, the system then experiences a reverse bias.

2.5.2 Metal-Semiconductor-Metal

A junction allows for current to flow between the semiconductor. However, since electrons and holes are in close proximity of each other, the recombination of electron and holes cause the overall efficiency of the device to be low. To resolve this, we sandwich a semiconductor by two metal contacts. These metal contacts are selective contacts, allowing only either the electron or the hole to pass through the barrier to the metal, blocking the other. Fig. 2.4 is an energy diagram of the p-type semiconductor with the left contact being a hole-selective contact and the right an electron-selective contact [14]. When a forward bias is applied, the fermi energy level, E_F, separates into the Fermi energy level for the holes and the electrons E_{Fp} and E_{Fn} respectively. When a steady voltage is applied, holes stay on the left side of the semiconductor while the electrons stay on the right. This allows for less recombination, a higher current, and an overall higher efficiency.

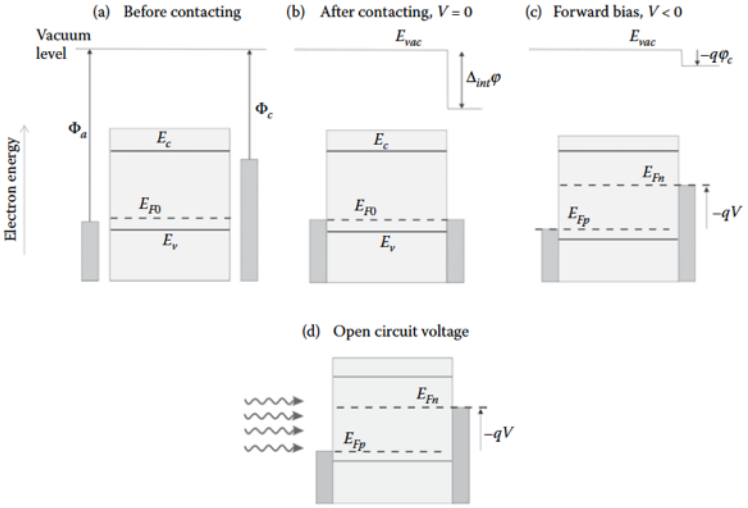

Figure 2.6: Energy diagram of what occurs to the energy levels within a semiconductor before being in contact of the two selective contacts, after contact, with a forward bias, and at open circuit voltage (voltage of the system not biased). Φ_a and Φ_c represent work functions of the hole-selective contact and electron-selective contact respectively. E_{vac}, and E_{F0} represent the energy for the vacuum and initial Fermi level at equilibrium. E_{Fn} and E_{Fp} represent the new Fermi energy level for the electron and holes, respectively, when a voltage, $-qV$, is applied. Finally, $\Delta_{int\Phi}$ is the work function change of the conduction band after contact and $-q\Phi_c$ is the work function change when $-qV$ is applied [14].

2.6 Characterizing Solar Cells

2.6.1 External Quantum Efficiencies

As stated at the beginning of the chapter, the semiconductors used in solar cells can only absorb certain wavelength of photons due to the size of their band gap. Silicon, perovskite, and organic solar cells absorb different ranges of wavelengths. Even if a material had a band gap which allowed for all of the sun's wavelength spectrum, the device itself can never be 100% efficient due to the Shockley-Queisser limit. The Shockley-Queisser limit states that due to the loss of energy through thermalization, barrier junction, contact resistance, and recombination, the highest limiting conversion efficiency (LCE) is 31% for solar cells [19]. While there is research being done trying to increase this number, the Shockley-Queisser limit is the convention [20]. Different types of solar cells are rated on their efficiencies with this. Using a mixture of light harvesting, charge generation, and charge collection, the external quantum efficiency (EQE) can be calculated by measuring the short-circuit current density (I/J_{SC}) as a function of wavelength [14] [1]. An example of an EQE curve is shown in Fig. 2.7.

2.6.2 JV Curves and Other Measured Properties

In order to understand how efficient solar cells are, we measure their currents at different applied voltages. These curves, as seen in Fig. 2.7, are current-voltage (IV) curves. The current of a device, should remain relatively consistent as voltage increases until a certain point, which differs between devices. Using this graph, I_{SC} and V_{OC} of a device can also be found. I_{SC} is the maximum current of a cell and occurs when the voltage across the device is zero. V_{OC} occurs when I_{SC} equals zero. Maximum power, P_{max}, occurs at the the maximum current point, I_{mp}, and maximum voltage point, V_{mp}, and can be found using the following equation [14]:

$$P_{max} = I_{mp}V_{mp}, \tag{Eqn. 2.1}$$

The quality of the solar cell, or the fill factor, FF, can be found using the following [14]:

$$FF = \frac{I_{mp}V_{mp}}{I_{SC}V_{OC}}, \tag{Eqn. 2.2}$$

The power conversion efficiency (PCE), η, is found by using the following equation [21]:

$$\eta = \frac{I_{SC}V_{OC}FF}{P_{IN}}, \tag{Eqn. 2.3}$$

where P_{in} is the input power.

---

[1] While we use current, I, throughout this chapter, it is important to note that many researchers use current density, J, instead. J is equivalent to current per unit area of a solar cell.

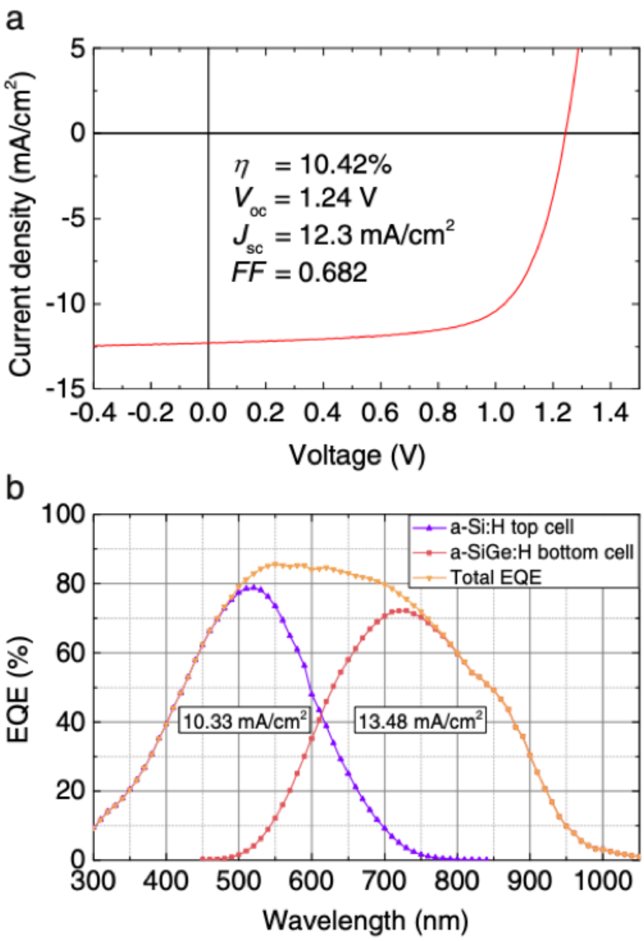

Figure 2.7: Graphs for a) JV curve of a tandem silicon solar cell, including η, V_{OC}, J_{SC}, and FF, and b) EQE of tandem cell, including EQEs of each half of the tandem cell [22].

2.7 Perovskite Solar Cells and Organic Photovoltaics

Table 1 shows a comparison of a few measured properties between silicon solar cells, PSCs, and OPVs. While PSCs have relatively high efficiencies compared to Si, the area of a typical PSC cell is on order of magnitude smaller. OPVs still have considerably low efficiencies and typically small areas. In addition to the small areas, PSCs and OPVs are not stable outside of lab conditions, and both do not maintain their efficiencies over a realistic timeline. There is still more research to be done on these solar cells, which can be done through modeling and imaging. The following chapters will expand upon how we used drift-diffusion analytical modeling to better characterize a layer in PSCs and how we used high-spatial-resolution thermoreflectance imaging to detect defects in OPVs.

Cell Classification	PCE (%)	Area (cm^2)	V_{OC} (V)	J_{SC} (mA/cm^2)	FF (%)
Si (crystalline)	26.7 ±0.5	79.0	0.738	42.65	84.9
Perovskite	20.9 ±0.7	0.991	1.125	24.92	74.5
Organic	11.2 ±0.3	0.992	0.780	19.30	74.2

Table 1: Comparison of Si solar cells, PSCs, and OPVS. PCEs measured under 1 sun (1000 W/m^2) at 25 C. Adapted from "Solar Cell Efficiency Tables (Version 54)" by Martin A. Green, et. al [23].

3 Modeling Spiro-OMeTAD using Drift-Diffusion Software

As mentioned in the previous chapter, some solar cells can have reduced efficiencies due to defects. However, perovskite solar cells (PSCs) actually use defects to help increase their charge carrier mobility, conductivity and efficiency. This chapter looks at what happens to the hole mobility in PSCs when the hole-transport layer, Spiro-OMeTAD, is doped. Typically, in order to understand the charge carrier mobility in solar cells and in their layers, people use over-simplified analytical models which do not take into account what happens when a layer is doped. Using a drift-diffusion model, we characterize the transition behavior between different doped states in Spiro-OMeTAD and investigate the effect of doping on its mobility and charge-carrier density. We found that this drift-diffusion model is a more accurate depiction of hole mobility than simplified analytical models.

3.1 Perovskite Solar Cells

PSCs are impressive because of their relatively high PCEs, the potential for using low-cost materials, and much more. Perovskite is a crystal structure in the form ABX_3.This particular perovskite is a lead base halide, where A is an inorganic compound (in the figure here CH_3NH_3), B is lead, and X is a halide, as seen in Fig. 3.1. Depending on the halide, PSCs can have a band gap can between 1.55 and 3.0 eV [24,25].

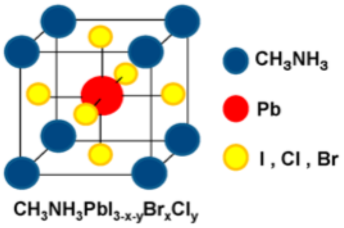

Figure 3.1: Crystal structure of methyl ammonia lead halide perovskite [26].

3.1.1 PSCs Energy-level Structure

Fig. 3.2 shows an energy level diagram for a PSC. For this device, the anode is fluorine tin oxide (FTO) and the cathode is gold (Au). The electron transport layer is titanium dioxide (TiO_2) and the hole transport layer is Spiro-OMeTAD. As explained in chapter two, a photon at the precise wavelength can excite an electron in the valence band of the perovskite layer into the conduction band, leaving behind a hole. The electron moves through the electron transport layer toward the anode, while the hole moves through hole transport layer toward the cathode. During PSCs original development in 2009, they had relatively low efficiencies due to the use of a liquid electrolyte for the hole-transport layer (HTL) [10]. It was in 2012, when researchers switched to using a solid-state hole-transport layer specifically, Spiro-OMeTAD, that the efficiencies of PSCs increased dramatically [10].

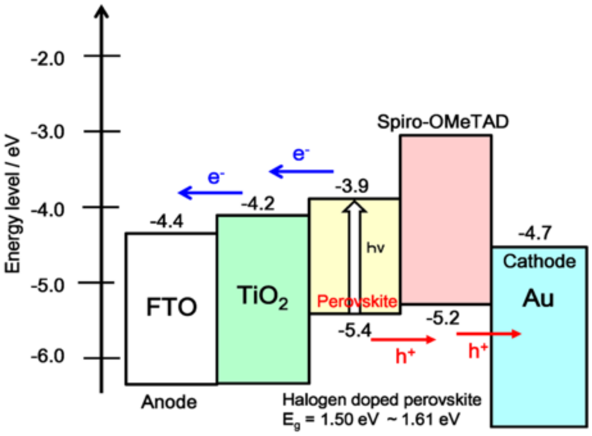

Figure 3.2: Energy level diagram for a solid-state PSC [41].

3.1.2 Spiro-OMeTAD

Spiro, seen in Fig. 3.3, is an amorphous organic semiconductor often used as the HTL in perovskite solar cells [27] because of its processability from common solvents and its ability to form smooth films that do not react with the perovskite layer. When first using Spiro as the HTL, the overall efficiency of PSCs increased by over 9% [10]. Spiro conductivity increases by a factor of two when it is doped with a lithium salt, lithium bis (trifluoromethyl sulphonyl) imide (LiTFSI), the structure of which is shown in Fig. 3.4 [28]. The lithium cations react with oxygen and Spiro, generating oxidized Spiro while the anion $TFSI^-$ stabilizes the oxidized Spiro [29].

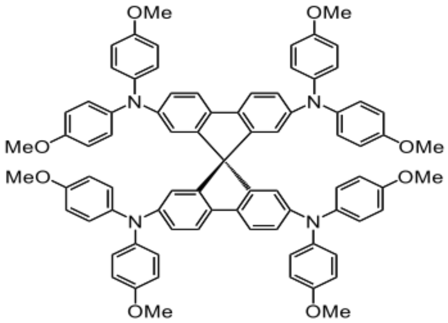

Figure 3.3: Spiro molecular structure [30].

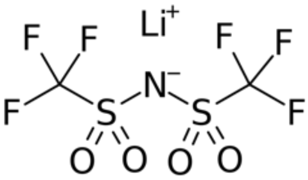

Figure 3.4: Lithium salt molecular structure. Adapted from J.A. Rohr paper on Spiro-OMeTAD [30].

While Spiro and the hole mobility in Spiro have been thoroughly characterized in its pristine state, LiTFSI-doped Spiro-OMeTAD is not well understood. It has been proposed that the mobility increases with doping density, but this was concluded based on simplified models [30] discussed later in the chapter.

3.2 Measuring Spiro

3.2.1 Single-Carrier Devices and Space-Charge-Limited Currents

Typically, Spiro is characterized in symmetric single-carrier devices (SCDs). SCDs sandwich a semiconductor, in this case Spiro, with either electron or hole selective metal contacts. The contacts have the same work function, making the device symmetric and allowing for there to be no built-in voltage [31]. When a small voltage is applied, only one charge carrier is injected into the semiconductor, allowing the transport to be dominated by one carrier type [31]. With enough voltage, charge carrier transport is dominated by drift as seen Fig. 3.5. An increase in voltage increases the charge carrier mobility in the device. The complete SCD for Spiro is seen in Fig. 3.6. Since Spiro is the HTL, the metal contacts used are hole selective contacts. SCDs are characterized with space-charge-limited current (SCLC) measurements, where the current is dominated by the charge carriers injected from contacts, to determine their charge-carrier mobility and doping density.

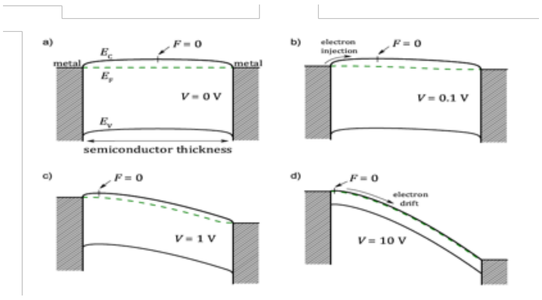

Figure 3.5: a) Symmetric electron-only device (SED) at thermodynamic equilibrium; b) SED with small voltage applied with electron injection; c) SED with enough applied voltage to have slight drift-dominant transport; d) SED with enough applied voltage for electron drift to occur. Hole-only devices are completely analogous. Adapted from J.A. Rohr paper on Spiro-OMeTAD [30].

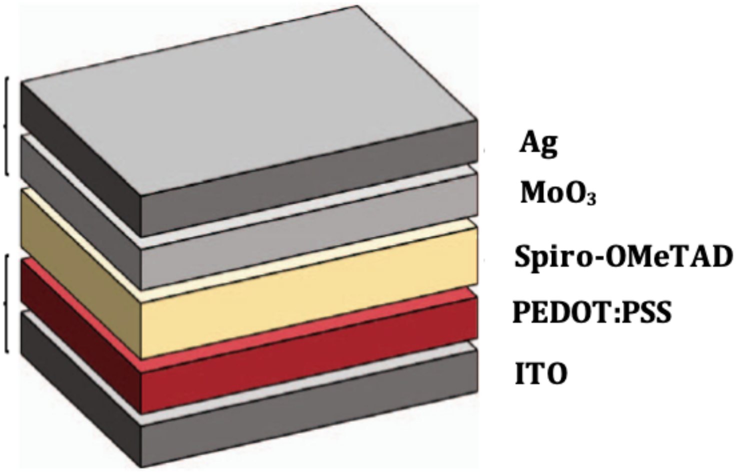

Figure 3.6: Symmetric hole only SCD. Adapted from J.A. Rohr paper on Spiro-OMeTAD [30].

3.3 Modeling

3.3.1 Typical Analytical Modeling

The analysis of SCLC measurements is often performed by fitting to over-simplified analytical models such as the Mott-Gurney's Law:

$$J = \frac{9}{8}\mu_n \epsilon_r \epsilon_0 \frac{V^2}{L^3}, \qquad \text{(Eqn. 3.1)}$$

or Ohm's Law:

$$J = nqv_d, \qquad \text{(Eqn. 3.2)}$$

where J is current density, μ_n is charge carrier mobility, ϵ_r is the static relative permittivity, ϵ_0 is the free space permittivity, V is the voltage applied, L is the length of the device, n is number of charge carrier, q is the charge of the electron, and v$_d$ is the drift velocity. While these equations work well with undoped SCDs, Eqn. 3.1 and Eqn. 3.2 do not account for defects and any doping in devices. As stated in Section 1.3.1, the change in voltage bias applied to the devices changes the charge carrier mobility, not the charge carrier concentration. The charge carrier mobility in Eqn. 3.1 is a known value depending upon the material, and not something that should change.

3.3.2 Drift-Diffusion Modeling Software

We use a drift-diffusion model software called General-Purpose Photovoltaic Device Model (GPVDM) in order to analyze our data. The drift-diffusion equations are as follows:

$$-\frac{J_n(x)}{q} = -D_n \frac{dn(x)}{dx} - n(x)\mu_n F(x), \qquad \text{(Eqn. 3.3)}$$

$$\frac{J_p(x)}{q} = -D_p \frac{dp(x)}{dx} + p(x)\mu_p F(x), \qquad \text{(Eqn. 3.4)}$$

where D$_{(n/p)}$ is the Einstein diffusion constant, n/p(x) is the electron/hole concentration at position x, $\mu_{(n/p)}$ is the electron/hole mobility, and F(x) is the force exerted. The first expression on the right side of each equation represents the effect of charge carrier diffusion in the direction of decreasing charge carrier concentration. It separates the changing variable, charge carrier concentration, from the charge carrier mobility, letting mobility stay unchanged. This allows us to more accurately describe what happens to a material when you change the charge carrier concentration by doping.

GPVDM solves both drift-diffusion equations (Eqn. 3.3 and 3.4) to characterize the movement of charges in a device and allows us to create current-density voltage (JV) curves.

3.4 Results

3.4.1 Proof of Concept

Using this model, we were able to fit the drift-diffusion model to experimentally measured JV curves of Spiro SCDs to by adjusting different device parameters in the software, such as electron or hole mobility, trap density, doping density and more [2]. Fig. 3.7 explores how JV curves, charge carrier density, and mobility are affected when keeping the exponential tails from Density of States (DOS) and removing them. DOS tell how many states there are in each energy level. This is typically represented as a gaussian distribution with the exponential tails which represent the energy levels in between the conduction and valence band of a material. We found that with the exponential tails, the JV curves were shifted lower than without exponential tails (Fig. 3.7.a). The exponential tails' charge carrier density is relatively stable as we increase doping density, but it decreases without them (Fig. 3.7.b). Finally, with exponential tails, the mobility increases as doping density increase and is shifted much lower than the no-exponential tail graph (Fig. 3.7.c).

---

[2] See Appendix A for more about GPVDM Software.

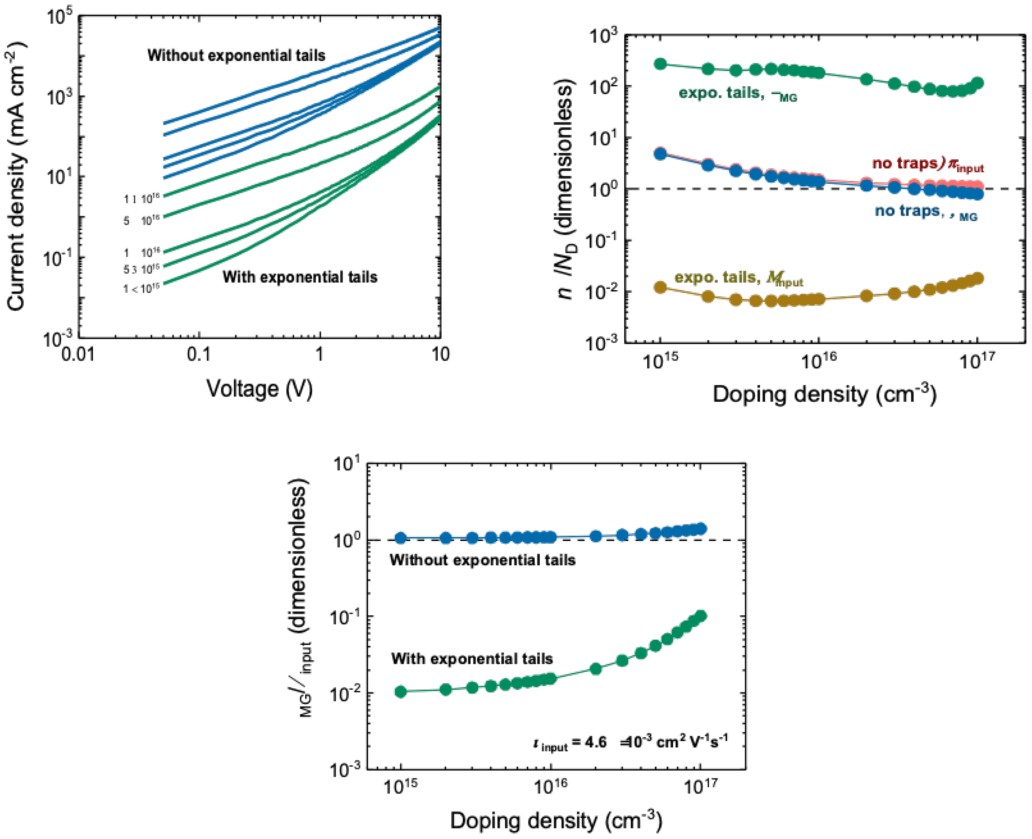

Figure 3.7: a) GPVDM JV curves; b) Charge-carrier density obtained from Ohm's Law/input doping density; c) GPVDM-calculated hole mobility/input mobility versus doping density. This data shows the effect of adjusting different device parameters.

3.4.2 Comparing Software to Typical Analytical Models

We compared the JV curves created from GPVDM to the JV curves measured in Spiro-OMeTAD devices, doped with LiTFSI at different amounts. In order for the LiTFSI to start its reaction with Spiro-OMeTAD, it had to be exposed to air and sunlight for different amounts of time. As the amount of time the device was in air and sunlight increased, so did the doping density. We found that the model curves (black lines in Fig. 3.8.a) closely followed the experimental data (colored circles).

Finally, we compared how charge carrier density and hole mobility found using GPVDM compared to finding them using Ohm's Law and Mott-Gurney's Law respectively. Fig. 3.8.b shows charge carrier density change more and at a higher density using Ohm's Law versus the model software.

As shown in Fig 3.8.c, when we increase the doping in our devices, Mott-Gurney's Law shows that mobility increases with doping by a factor of 100. GPVDM shows that the mobility, no matter the doping, remains in a similar range, not even increasing with doping by a factor of 10.

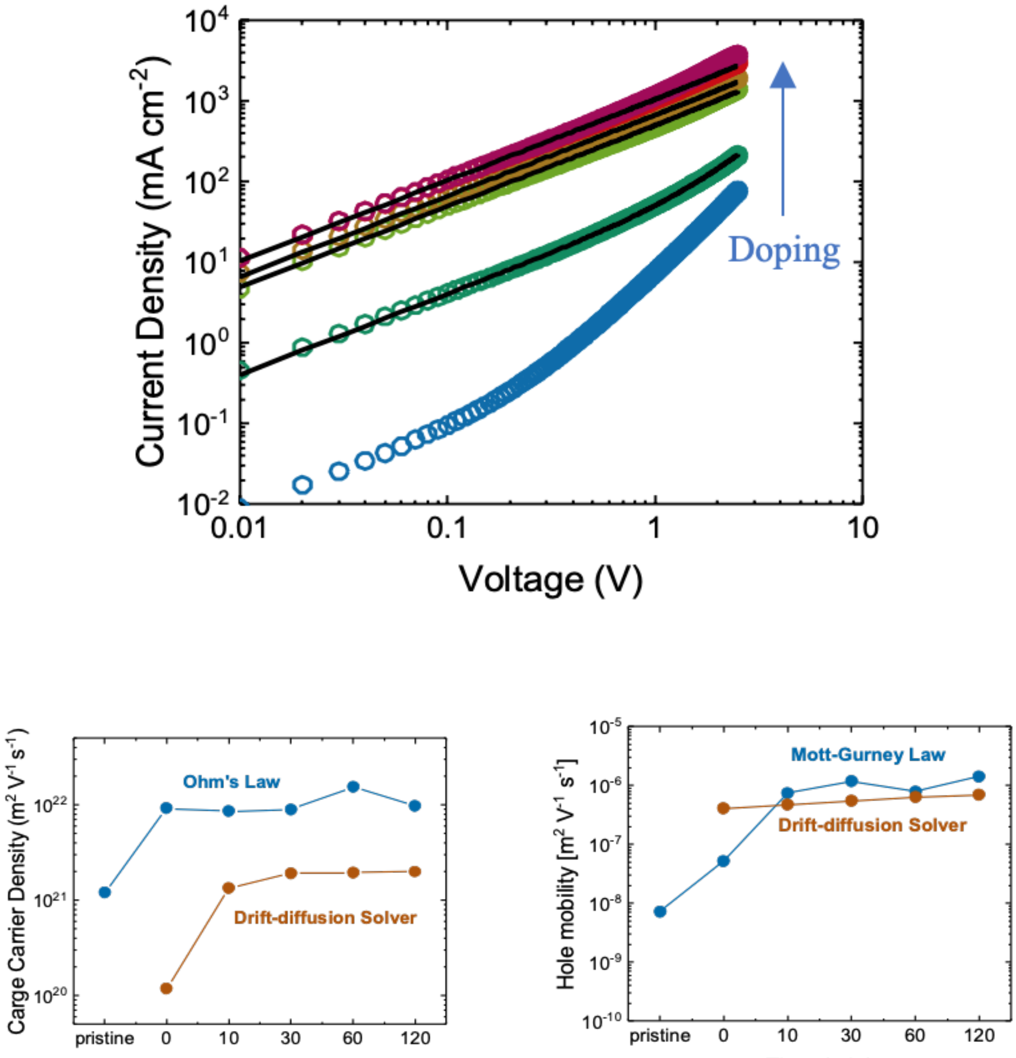

Figure 3.8: a) Comparing GPVDM and experimental data JV curves; b) Charge-carrier density obtained from Ohm's Law versus time; c) GPVDM-calculated hole mobility/ input versus time. Time is a proxy for doping density and denotes how long the device has placed in the sun and air.

3.5 Conclusion

We use GPVDM to understand charge-transport in Spiro-OMeTAD hole transport-only devices, giving precise values for the hole-mobility and charge-carrier concentration. As doping increases, GPVDM shows that the hole mobility in a device remains steady (Fig 3.8.c). We plan to use this knowledge to accurately model perovskite solar cells in the future.

4 Characterizing Defects in Organic Photovoltaics using Thermoreflectance Imaging

The previous chapter looked at how to characterize layers in solar cells to better understand how it functions. This is important in finding how defects can initially affect the system. This chapter looks at the defects that may come about through the process of creating a full solar cell. We used a particular kind of imaging, thermoreflectance imaging, on organic photovoltaics, to identify and characterize defects in the whole cell.

4.1 Organic Photovoltaics

Thin-film Organic Photovoltaics (OPVs), like perovskites solar cells (PSCs), are intriguing because of their flexibility, tunable material properties, and potentially low cost [12]. What is even more incredible is how swiftly their PCE's have increased through research. In 2001, OPVs had only a 2.5% efficiency, but in 2018, by creating tandem solar cell between two different OPVs, researchers were able to reach 17.3% efficiency [12,31]. Though not close to reaching the efficiencies of perovskites and silicon cells, the speed at which research for this particular solar cell has been progressing, combined with the potential for novel applications due to their mechanical flexibility, shows the potential for OPVs.

4.1.1 OPV Structure

The energy level diagram of the OPV used for this research is shown in Fig. 4.1. This is an inverted cell since the light is coming in through the cathode instead of the anode. For this device, the cathode is indium tin oxide (ITO) and the anode is silver (Ag). The electron transport layer is zinc oxide (ZnO) and the hole transport layer is Poly (3,4-ethylenedioxythiophene) polystyrene sulfonate (PEDOT:PSS) and molybdenum trioxide (MoO_3), the dashed line. Finally, the active layer of the device is a mixture of poly (3-hexylthiophene-2,5-diyl) (P3HT) and phenyl-C61-butyric acid methyl ester (PCBM).

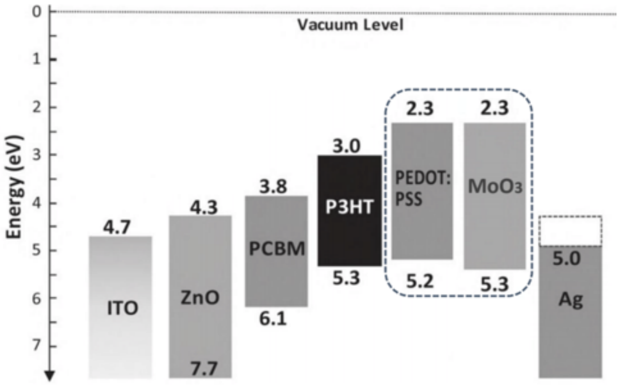

Figure 4.1: Energy level diagram of the specific OPV used in this thesis [32].

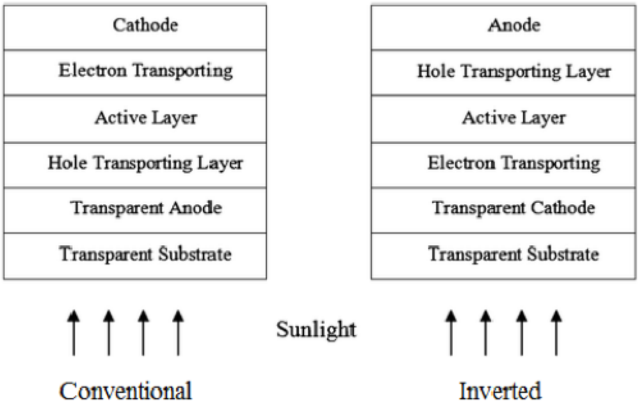

Figure 4.2: A Layout of a conventional solar cell compared to an inverted one. Note, we use glass as our transparent substrate. [33].

Fig. 4.3 shows a characteristic IV curve for an aged cell, a cell which has been biased by voltage or sunlight multiple times, is shown, under both completely dark (blue line) and illuminated (orange line), with a light source roughly equivalent to one “sun”, conditions. The dark condition occurred by covering the whole cell with a dark black cloth, ensuring no light could come in contact with it. Simulating one sun was done by using a sun lamp, such as one used for plants, which mimics the solar spectrum but is uncalibrated.

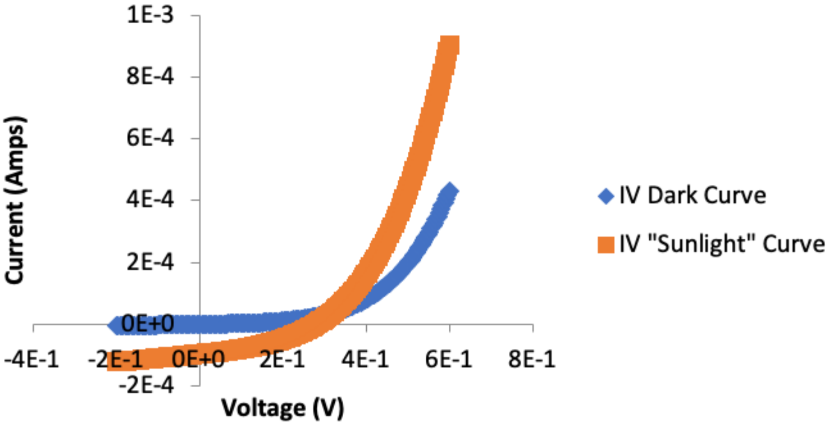

Figure 4.3: Measured IV curves of an OPV under dark (blue) and illuminated, equivalent to one "sun" (orange) conditions.

4.1.2 Comparing OPVs to Silicon and PSCs

As stated previously, OPVs are promising because of their potential to be flexible, in contrast to silicon solar cells, which are rigid because of the silicon crystal used for their active layer. However, OPVs have an extremely short carrier lifetime or the amount of time a charge carrier can move before recombining. This short carrier lifetime decreases the overall efficiency of the cell. Fig. 4.4 is a graph which compares different types of solar cells short-circuit current density (J_{SC}) versus open-circuit voltage (V_{OC}) x fill factor (FF) [34]. The graph also shows how close a solar cell's efficiency is to the Shockley-Queisser limit (ηSQ). This shows that OPVs' efficiencies are significantly further from ηSQ than that of commercial silicon solar cells and even PSCs.

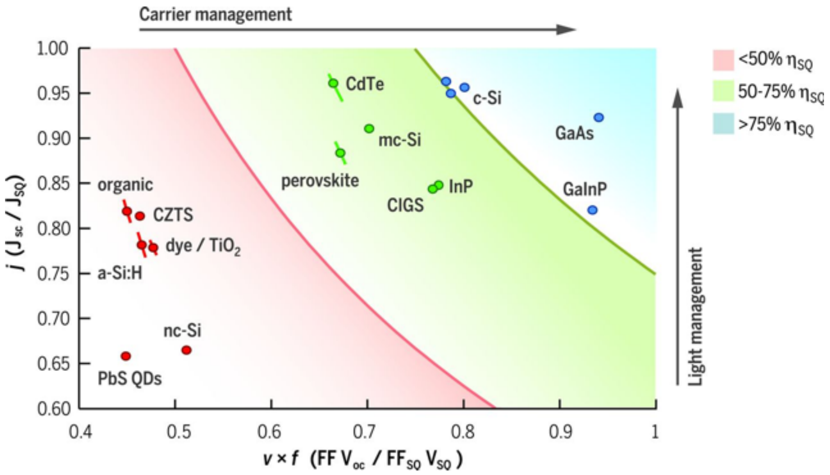

Figure 4.4: Measured solar cell's voltage x fill factor versus their current density. This graph compares different types of solar cells carrier management. The percentage of the η_{SQ} (Shockley-Queisser limit) represents how close the solar cell efficiency is to the Shockley- Queisser limit. OPVs' efficiencies are much further from the η_{SQ} to silicon and PSCs. [34].

4.1.3 Defects in OPVs

Defects or shunts also have a huge influence on the efficiency of OPVs. In previous research on silicon solar cells, it has been found that there are nine types of shunts, six of which are processed-created and three that are in-grown defects from the materials [35]. Two most common shunts found in Si cells are linear (resistor-like) and nonlinear (diode-like) shunts. Linear shunts can be found with both forward and reverse bias voltage whereas nonlinear shunts can only be found with forward bias. Shunts typically occur at a hotspot on a device or an area on the device where the heating is significantly higher in a localized area compared to its surroundings, see Fig. 4.5 for an example. At localized hotspots, there can be a potential for irreversible damage, thus bringing down the overall efficiency of a cell.

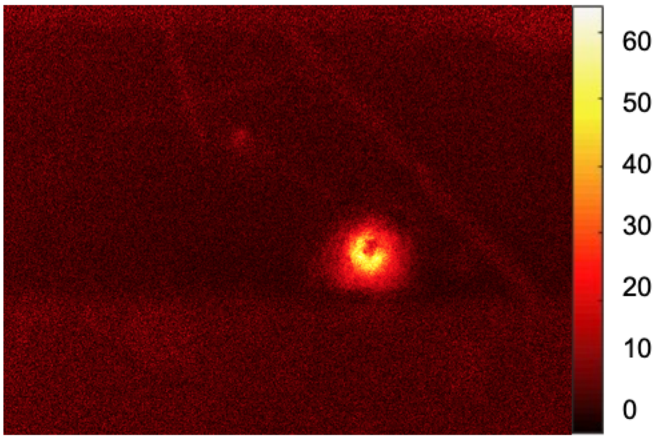

Figure 4.5: Example of a hotspot on an OPV found using Thermoreflectance imaging.

4.2 Thermoreflectance Imaging

Most commonly, defects are found using such as photoluminescence imaging or lock-in infrared thermography. Thermoreflectance is another type of imaging that has been shown to identify different types of shunts in conventional silicon solar cells. In this work, our goal is to extend this work to characterize defects in organic solar cells and identify their physical origins using thermoreflectance imaging.

4.2.1 Conventional Imaging Techniques

Besides thermoreflectance imaging, there are a few other imaging techniques typically used to detect shunts in solar cells, specifically Si solar cells. Photoluminescence imaging works by illuminating the solar cell with an 804 nm wavelength irradiation, set electrically to certain operating conditions [36]. Then a Si-charged coupled device (CCD)-camera collects the emitted luminescence radiation. Fig. 4.6 shows a typical set up for PL imaging, while Fig. 4.7 shows results using the technique. While PL imaging does allow for some defects to be seen, they do miss some shunts that can be seen using lock-in infrared thermal (LIT) imaging [37].

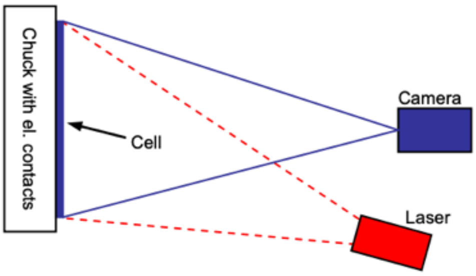

Figure 4.6: Typical setup for photoluminescence imaging where a laser of certain wavelength irradiates the cell and a CCD-camera collects the emitted radiation [36].

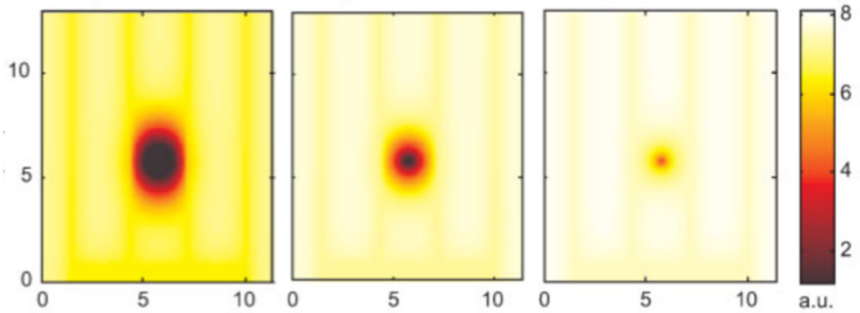

Figure 4.7: Example of a shunt on a Si solar cell found using PL imaging [38].

Conventional LIT imaging allows for non-contact thermal mapping of solar cells by biasing the cell with a pulse trigger and capturing the change in temperature with an infrared camera [39]. One large issue with LIT imaging is that is limited to a resolution of 4-6 microns, such that smaller pinpoint shunts are difficult to identify using this technique [35]. Fig. 4.8 shows a typical set up for LIT imaging, while Fig. 4.9 shows results using the technique.

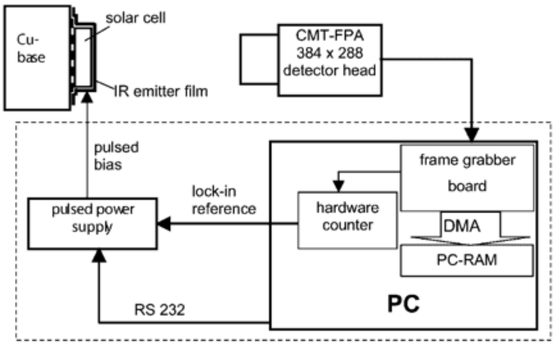

Figure 4.8: Typical setup for lock-in infrared imaging where a pulse trigger biases the cell and an infrared camera collects the resulted change in temperature [39].

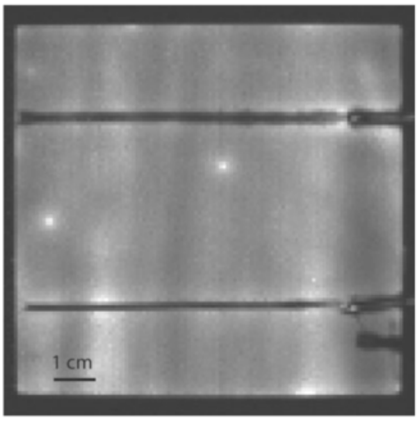

Figure 4.9: Example of a Si solar cell found using LIT imaging in grayscale [39].

In our work, we use a thermoreflectance imaging technique that provides non-contact, high resolution 2D thermal imaging and energy mapping with demonstrated spatial resolutions of up to 250nm.

4.2.2 Thermoreflectance Imaging Technique

The thermoreflectance imaging technique relies on the temperature dependence of the refractive index, such that a small change in temperature (ΔT) causes a small change in the relative reflectivity (ΔR/R) of a material. Fig. 4.10 and Fig. 4.11 show an image of a typical thermoreflectance setup as well as an amplitude and phase image of a shunt in a silicon solar cell.

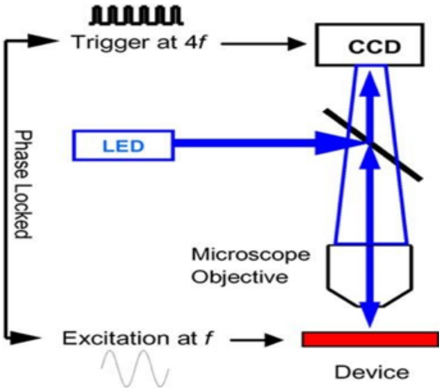

Figure 4.10: Typical thermoreflectance setup [40].

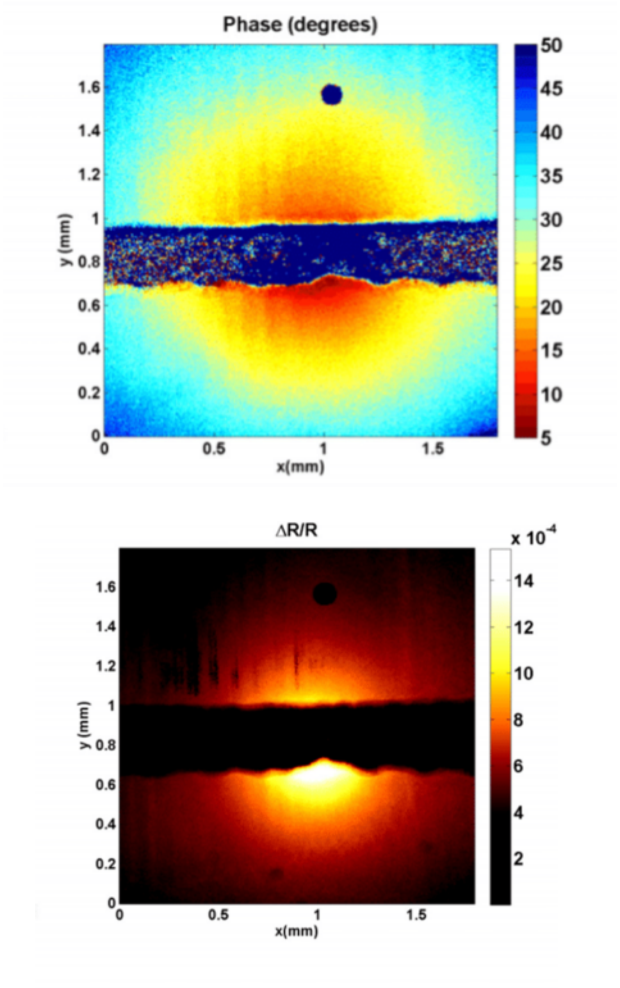

Figure 4.11: a) Thermoreflectance amplitude of a silicon solar cell, and b) the phase image of the measured hot spots [40].

To acquire a thermal image of a solar cell, the cell is electrical biased at modulated frequency f, resulting in a temperature modulation at frequency f and $2f$. The thermal modulation in turn causes small changes in the reflectivity which can calculated using Eqn. 4.1:

$$\frac{\Delta R}{R} = \kappa \Delta T, \qquad \text{(Eqn. 4.1)}$$

where $\kappa \approx (10^{-3}$ - 10^{-6} K$^{-1})$ depending on the material that is being reflected against [41].

A camera then collects images at frequency $4f$ during a certain modulation period. During this period, the four measured intensities for each pixel are summed in “buckets” (I_k) over many iterations. From the four buckets, high resolution amplitude (ΔR/R) and phase images of the relative change in reflectivity at frequency f can be calculated using Eqns. 4.2 and 4.3:

$$\Phi = \arctan(\frac{I_1 - I_2 - I_3 + I_4}{I_1 + I_2 - I_3 - I_4}) - \Psi, \qquad \text{(Eqn. 4.2)}$$

$$\frac{\Delta R}{R} = \frac{\pi}{\sqrt{2}} \frac{\sqrt{(I_1 - I_3)^2 + (I_2 - I_4)^2}}{I_1 + I_2 + I_3 + I_4} = \frac{\Delta}{c}, \qquad \text{(Eqn. 4.3)}$$

where Φ is the phase delay of each pixel, Ψ is phase effect caused by delays from electronics and anything else used, Δ is the amplitude of the changing reflectivity of the DC reflectivity, and c is the DC reflectivity [42].

4.3 Results

4.3.1 Proof of Concept

We use a gold micro-resistor of 134.5 to test our thermoreflectance imaging technique. We bias the resister under varying electrical bias modulation depths between 10-50 mA, each image taken for 20,000 iterations. Typical results for the thermoreflectance amplitude and phase images of the relative change in reflectivity ΔR/R are shown in Fig. 4.12. In the amplitude image, (Fig. 4.12.a) the area of the micro-resistor which is heated is the only place where there is a significant increase the micro-resistor’s reflectivity. And in the phase image, only does the heated area have a uniform signal (Fig. 4.12.b), proving that the camera has successfully locked in on the correct area. Finally, we find that ΔR/R of the micro-resistor scales linearly electrical bias power (W), as expected. The gold micro-resistor thus proves that our thermoreflectance imaging setup is successful and allows us to use the technique on OPVs.

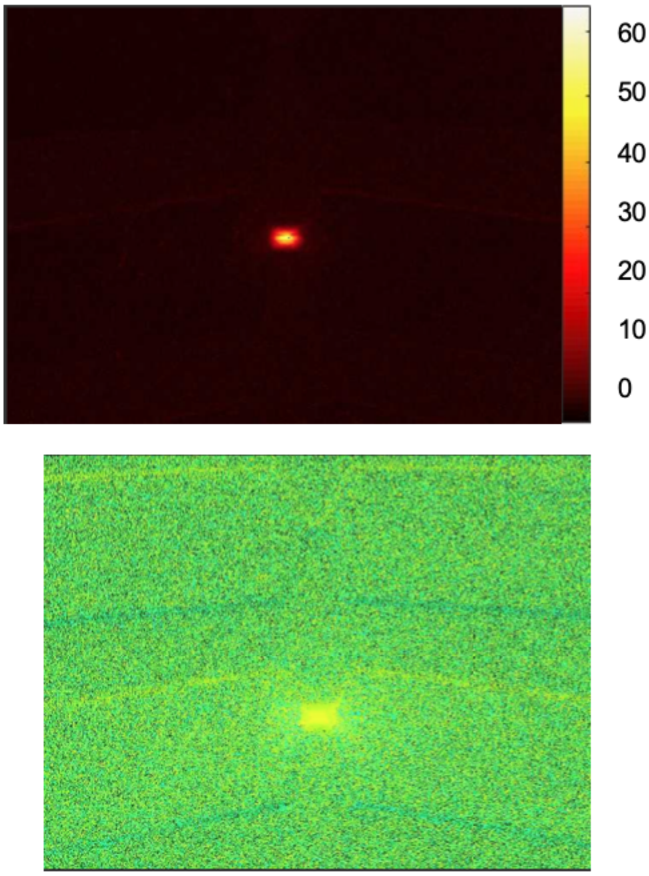

Figure 4.12: Measured a) thermoreflectance amplitude and b) phase of the relative change in reflectivity of a gold microresistor in response to heating resulting from electrical bias modulation.

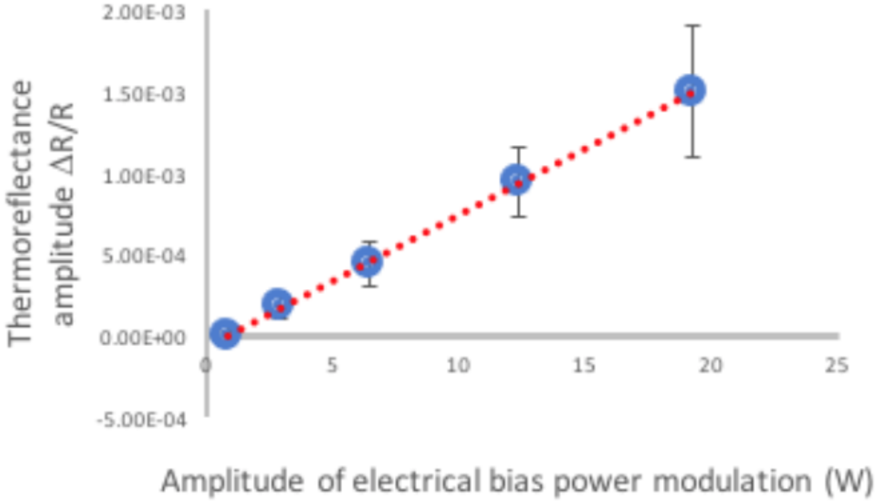

Figure 4.13: The thermoreflectance amplitude ΔR/R scales linearly with electrical bias power [43].

4.3.2 Defects Found in Devices

Using thermoreflectance imaging, we identify a hot spot from electrical shunts in test OPV cells, seen in Fig. 4.14. The cell, created by Sabrina Li (PO '17), is electrically biased varying voltage instead of current. The electrical bias modulation depths are between 500mV-1V, each image taken for 50,000 iterations. Fig. 4.14.a is an optical image of the cell. Fig. 4.14.b is a thermoreflectance amplitude image of the cell. Unlike the amplitude image of the micro-resistor, it is not only the localized hotspot with a ΔR/R than the rest of the cell. The entire cell left of the crack has a slight increase in ΔR/R as well, though not as large as the localized hotspot itself. Fig. 4.14.c is a phase image of the cell. While the localized hotspot is the most uniform of the cell, once again the rest of the cell is slightly more uniform than its surroundings. However, because the hotspot is the most uniform area in the phase image, we can still say that the thermoreflectance technique works.

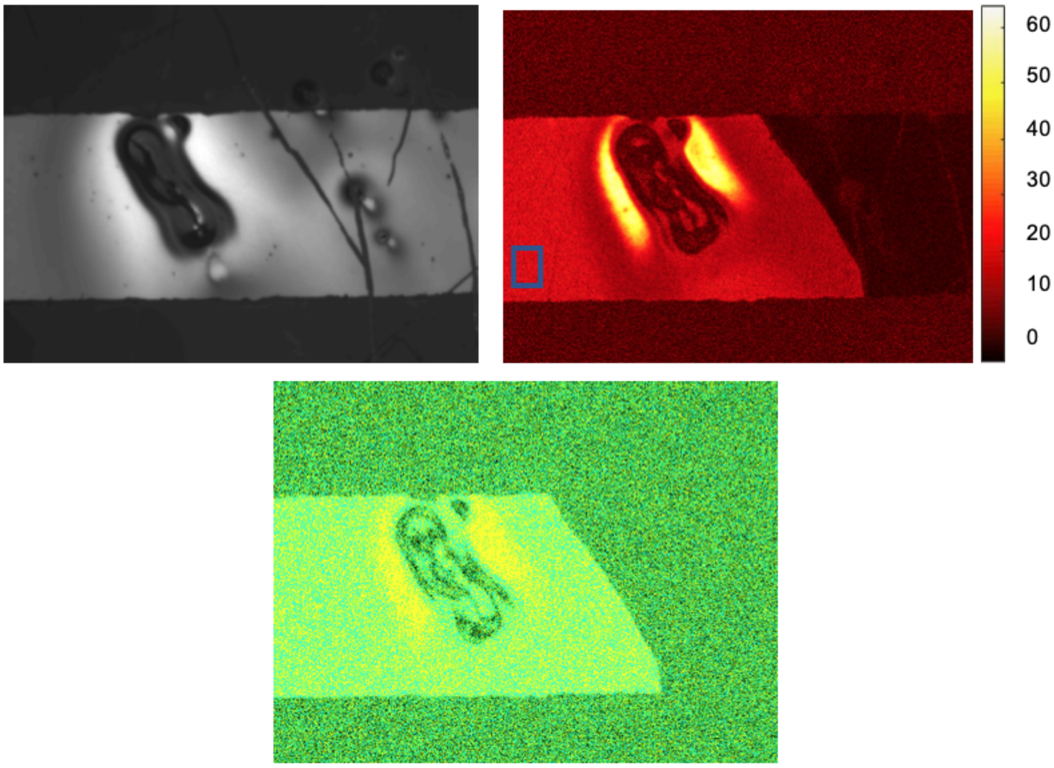

Figure 4.14: a) Standard optical top-down image of an organic solar cell in grayscale, thermoreflectance amplitude b) and phase image c) of the measured hot spots. The blue box in b) indicates the region of the cell that was analyzed to quantify background heating (see Section 4.3.3).

Identifying Types of Defects

To identify the physical origin of the shunts, we measure the temperature of multiple hot spots under varying electrical bias conditions described previously. Note that the hot spot in Fig. 4.14 is not a part of this set of data. Fig. 4.15 shows the trends of diode-like and resistor-like hot spots discussed in Section 1.1.3.

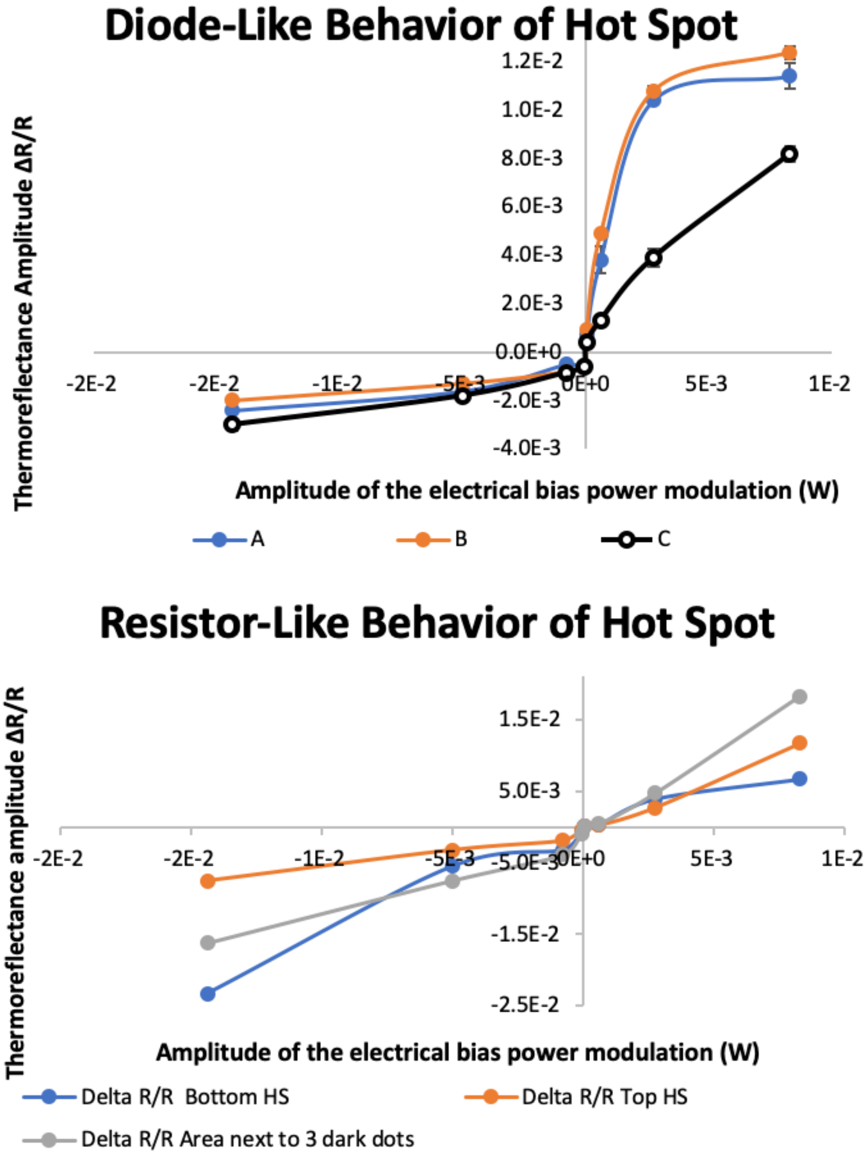

Figure 4.15: Measured temperature (ΔT ΔR/R) of the hot spot as a function of the amplitude of the modulation of the electrical bias power ΔP_{El} of three different hot spots; (a) a graph of a "weak diode-like" behavior, and (b) a graph of a "resistor-like" behavior.

4.3.3 Heating Issues

As noted previously, the thermoreflectance images of the biased solar cells appear to show background heating of the entire cell, even in regions away from the localized hot spots. If this is the case, then the measured change in reflectivity, $\Delta R/R$, which is proportional to ΔT, should scale with power, P. We examined a small background of the cell well away from a hot spot (see Fig. 4.11.b) and measured $\Delta R/R$ vs. voltage bias V and electrical power, ΔP_{el}. We found that there seems to be a linear relationship between $\Delta R/R$ and V, but $\Delta R/R$ does not scale linearly with ΔP_{el}, suggesting that the background signal may have a physical origin other than heating. There are a few possible tests to do in order to see if the thermoreflectance signal arises from heating which can be found in Appendix B.

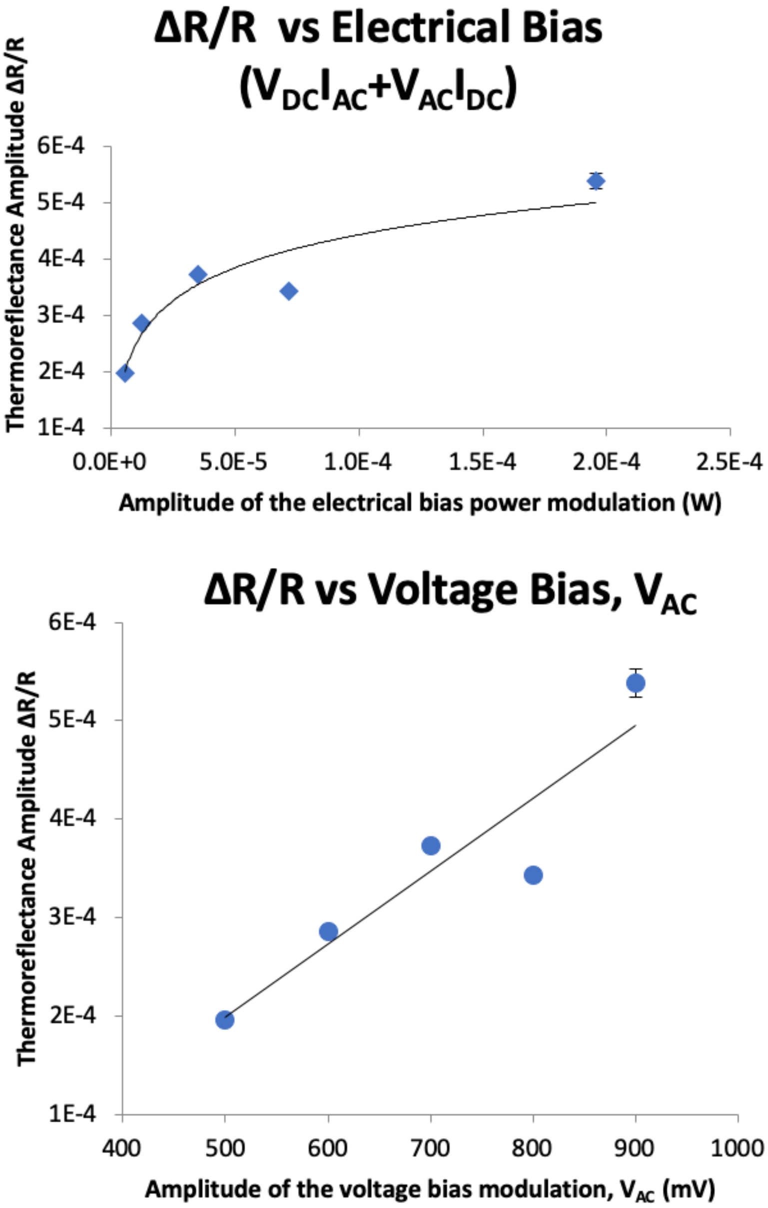

Figure 4.16: a) Measured ΔR/R of the hot spot as a function of the amplitude of the modulation of the electrical bias power ΔP_{el}. b) Measured ΔR/R of the hot spot as a function of the amplitude of the voltage bias modulation, V_{AC}.

4.4 Conclusion

We use thermoreflectance imaging to characterize defects in organic photovoltaics. We have successfully imaged hot spots and determined the behavior of different hot spots. Once we have determined why and how our measured thermoreflectance signals are showing whole-cell heating, we will compare our imaging measurements with more conventional means of characterization such as IV curves, light beam induced current measurements, and photoluminescence imaging. Ultimately, the goal of this project is to combine our results with more conventional means of characterization to develop a powerful suite of tools for characterizing the types and physical origin of defects present in OPVs.

5 Conclusion

Over the course of my thesis, I have looked at two ways to characterize solar cells. The first was through using a drift-diffusion software as a way to more accurately model hole mobility and hole carrier density in Spiro-OMeTAD, an important layer in perovskite solar cells (PSCs). The second was through thermal imaging of organic photovoltaics (OPVs) in order to identify and characterize defects within those devices.

5.1 Modeling Spiro-OMeTAD

Spiro-OMeTAD has been found to be a reliable and efficient hole-transport layer in a PSC. Typically, when the hole mobility in Spiro has been modeled and analyzed it has been through simplified mathematical analysis, such as Mott Gurney's Law (Eqn. 3.1) and Ohm's Law (Eqn. 3.2). While both of these are valid and conclusive when measuring pristine Spiro, or Spiro that has not been doped, these equations are ineffective when Spiro is doped. In contrast, drift-diffusion equations (Eqn. 3.3 and 3.4), which had an additional factor of change in charge carrier density, take into account the possibility of doping and are the basis for modeling doped Spiro.

The drift-diffusion equations, paired with a few other equations (see Chapter 3.4.2), were the backbone of the modeling software we used to model hole mobility and carrier density. The software, General-purpose Photovoltaic Device Model (GPVDM), allows us to input experimentally obtained voltage-current density data, and through solving the drift-diffusion equations, can fit a plot to the data given. The fit parameters, such as doping density, charge carrier concentration, exponential tail and more, can be varied as such to give us the most accurate output of a voltage-current density plot. Using the GPVDM, we were able to vary the doping density in the model, to mimic how one would dope Spiro, and see what would happen to its hole mobility and carrier density.

Using the software, we were able to see that hole mobility in Spiro does not increase as we increase the doping, which makes sense physically. This proved it to be more accurate than Mott Gurney's Law, which suggests that mobility should increase with doping. When looking at charge carrier density, we also found that, omitting the outlier of the first plot point (Fig. 3.8.a/b), it too did not change as doping was increased. This again showed that the software and using drift-diffusion equations was more accurate than Ohm's Law.

The next step for this project is to take more experimental data and use the software to try to fit the data in order to get a proper error range. Then, we would move onto modeling the whole PSC, to see how accurate of a model we could get from GPVDM. The drift-diffusion software is important because it allows for us to change parameters in our devices and see the effects of that almost immediately, compared to having to build the entire device. This could be beneficial when trying to make slight changes to PSCs to help make them even more efficient.

5.2 Imaging Organic Photovoltaics

While PSCs are nearly equal in efficiency to silicon solar cells in the lab, OPVs often have only half the efficiency of its competitors. One way people often try to understand what is limiting then efficiency of solar cells is by trying to locate defects or shunts through imaging. Typically, people use light-beam induced current (LBIC) or infrared (IR) imaging in order to find defects in cells. However, these imaging methods have relatively low-spatial resolution. Thermoreflectance (TR) imaging allows us to image cells with spatial resolution of 250 nm.

Using TR imaging we were able to locate defects, and, in previous studies, we were able to characterize shunts as diode-like and resistive-like. However, these were found when biasing the OPVs with too much current causing them to degrade much faster than they should, and eventually cracking and destroying the device. This time, we worked to bias the OPVs within a reasonable operating voltage range (between 0-1.5 V_{OC}). We were still able to find defects in the OPVs, and the devices last longer than in previous experiences. Yet, overtime there was still cracking of the cell.

We also found that when voltage biasing the device, we saw the entire cell heating in addition to the hotspots, something that had not occurred in the past. One of our next steps is to test to see the cause of our whole-cell heating, First, we plan to bias the cell once again with current, but in the proper range such that we do not see the OPV degrade as fast as it once did (see Appendix B on how to do this). Once we either understand why whole-cell heating is occurring or if there is a way to stop it, we want to continue to image OPV devices using TR imaging to collect more data.

Once we have determined the physical origin of our measured TR signals, we will compare our TR imaging measurements with more conventional means of characterization. Ultimately, the goal of this project is to combine our thermal imaging results with more conventional means of characterization to develop a powerful suite of tools for characterizing the types and physical origin of defects present in OPVs.

5.3 Impact

Over the course of my two projects, I have been able to learn about the intricacies of two different types of solar cells. I gained better understanding about the materials used to create them and their possible future applications. I have also learned two very powerful ways to characterize solar cells, including modeling hole transport mobility using drift-diffusion software and experimentally characterizing efficiency-limiting defects using thermoreflectance imaging. Complex modeling and device degradation will lead to better understanding of solar cells, thus allowing for more opportunities in for discovery in this technology.

A Using GPVDM Software

The General-Purpose Photovoltaic Device Model, created by Dr. Roderick Mackenzie at the University of Nottingham, uses drift-diffusion equations as well as other electrical and optical model to simulate different types of thin film devices. Some example of thin film devices already embedded in the system are perovskite solar cells, organic field effect transistors, and organic LEDs [44]. What is unique about GPVDM, compared to similar software, allows for anyone to build their own thin film devices from the ground up. The software simulates JV curves, impedance spectroscopy, ray tracing and more. We used the software to simulate JV curves, as well as understand the hole mobility and charge-carrier density of Spiro-OMeTAD.

A. General Setup of GPVDM Software

Fig. A.1 shows what the home interface of the GPVDM Software look like. The center screen shows the model of the SCD developed in the software, which can be created using the layer editor. The top and bottom contact mimic the hole-selective metal contacts on an experimental SCD, and the Spiro-OMeTAD is the active semiconductor layer in the SCD.

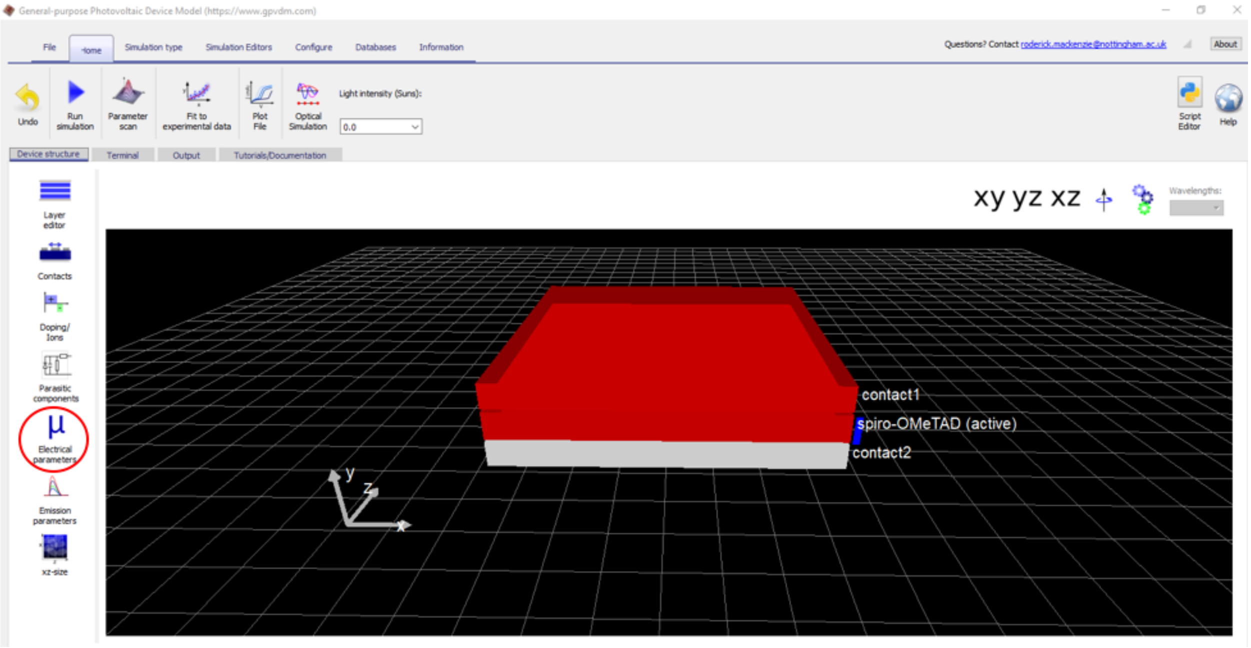

Light intensity (Suns): 0.0

Figure A.1: A shot of the GPVDM Software. Using the simulator, we built a hole only, Spiro-OMeTAD single carrier device.

The left panel are different parameters that can be edited to allow for the devices to be as accurate as possible. In this thesis we focus on changing the parameters in the Doping/Ions and the electrical parameters. The Doping/Ions allows for us to adjust how much the Spiro-OMeTAD is doped with LiTFSI. The electrical parameters, shown in Fig. A.2, are the parameters which focus on how the properties of the electrons and holes in the device. This is where we are able to see how the hole mobility and the charge carrier density (hole trap density) changes with doping.

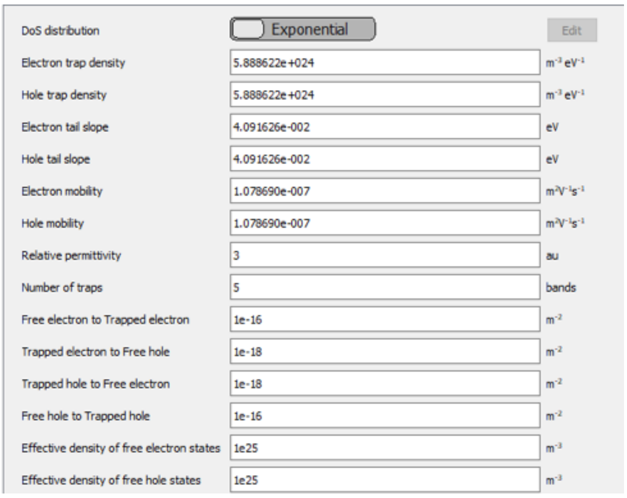

DoS distribution	Exponential	Edit
Electron trap density	5.888622e+024	m^{-3} eV^{-1}
Hole trap density	5.888622e+024	m^{-3} eV^{-1}
Electron tail slope	4.091626e-002	eV
Hole tail slope	4.091626e-002	eV
Electron mobility	1.078690e-007	m^{2}V^{-1}s^{-1}
Hole mobility	1.078690e-007	m^{2}V^{-1}s^{-1}
Relative permittivity	3	au
Number of traps	5	bands
Free electron to Trapped electron	1e-16	m^{-2}
Trapped electron to Free hole	1e-18	m^{-2}
Trapped hole to Free electron	1e-18	m^{-2}
Free hole to Trapped hole	1e-16	m^{-2}
Effective density of free electron states	1e25	m^{-3}
Effective density of free hole states	1e25	m^{-3}

Figure A.2: Parameters that can be adjusted in the electrical parameter settings.

B. Using “Fit to Experimental Data” Function

In order to find hole mobility and charge carrier density, we create JV curves on the software by fitting experimental data and allowing certain electrical parameters to vary. This is done through the “Fit to Experimental Data” function. First, we import experimental JV curve data into the software, as seen in Fig. A.3.a. Then, we “fix” the electrical parameter that we want to vary or not, by turning them on or not. As seen in Fig. A.3.b, the “on” indicates that these parameters will vary in order to fit the experimental data. After selecting which parameters to vary, in our case hole mobility and charge carrier density, we can select “Run Fit” and allow the software to fit the imported data. “Run Fit” creates a continuous number of JV curves, each time varying the necessary parameters until creating a JV curve very similar to the experimental data imported. Fig. A.3.c shows an example of one run completed by the software. The simulation JV curve in blue, is attempting to match the experimental data in green. The Delta in red, shows the difference between the two graphs. Once, Delta is a horizontal line at zero, we can stop the “Run Fit”, and export the

JV curve of the simulation. We can also go back to the electrical parameters settings and see the new hole mobility and charge carrier density. By increasing the doping density in Doping/Ions, we are able to get multiple JV curves, hole mobilities and charge carrier densities. These simulated JV curves are then compared to the experimental data, while the simulated hole mobilities and charge carrier densities are compared to simplified analytical models (Fig. 3.8).

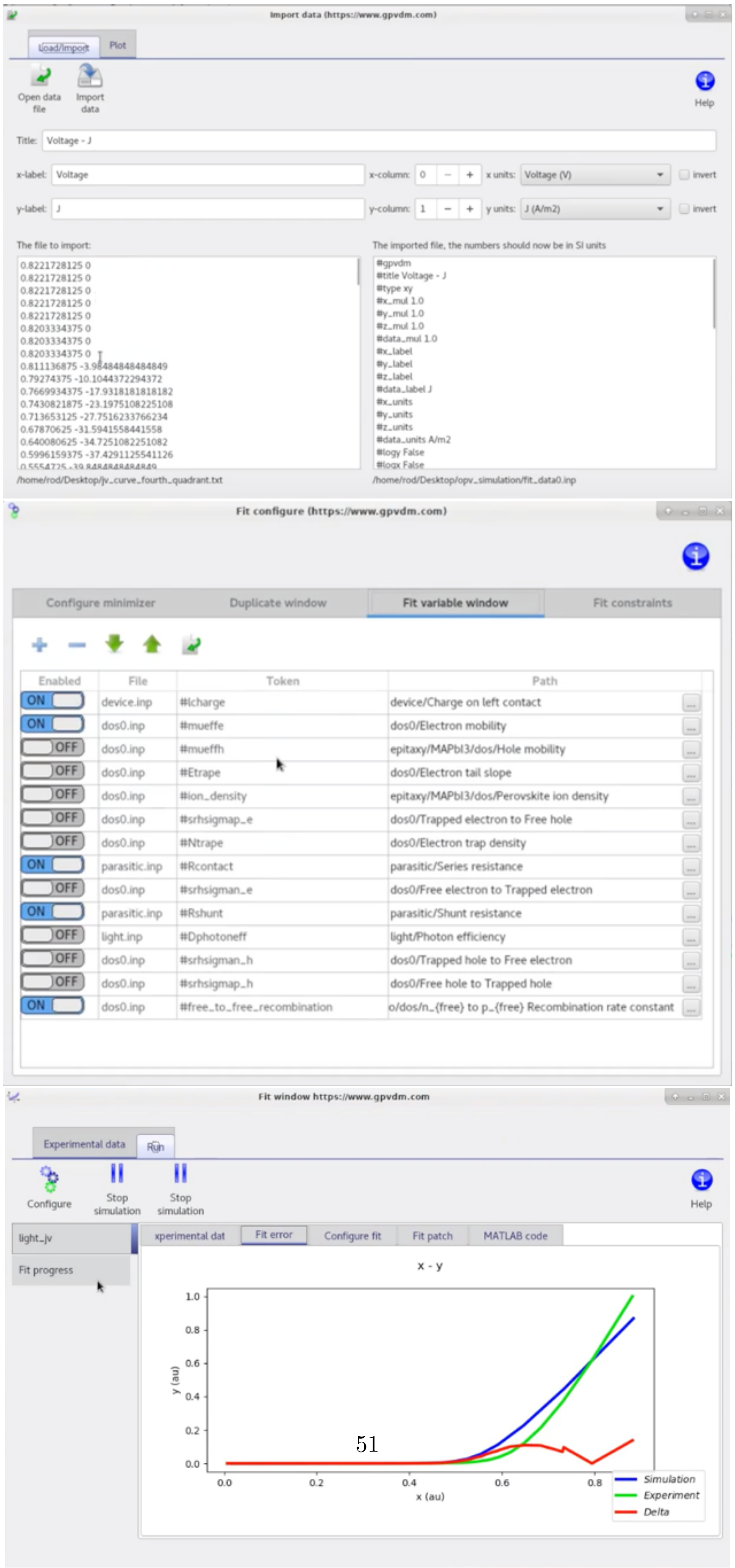

Title: Voltage - J

x-label: Voltage x-column: 0 x units: Voltage (V) ☐ invert

y-label: J y-column: 1 y units: J (A/m2) ☐ invert

The file to import:

```
0.8221728125 0
0.8221728125 0
0.8221728125 0
0.8221728125 0
0.8221728125 0
0.8203334375 0
0.8203334375 0
0.8203334375 0
0.811136875 -3.98484848484849
0.79274375 -10.1044372294372
0.7669934375 -17.9318181818182
0.7430821875 -23.1975108225108
0.713653125 -27.7516233766234
0.67870625 -31.5941558441558
0.640080625 -34.7251082251082
0.5996159375 -37.4291125541126
0.5554725 -39.8484848484849
```

/home/rod/Desktop/jv_curve_fourth_quadrant.txt

The imported file, the numbers should now be in SI units

```
#gpvdm
#title Voltage - J
#type xy
#x_mul 1.0
#y_mul 1.0
#z_mul 1.0
#data_mul 1.0
#x_label
#y_label
#z_label
#data_label J
#x_units
#y_units
#z_units
#data_units A/m2
#logy False
#logx False
```

/home/rod/Desktop/opv_simulation/fit_data0.inp

Enabled	File	Token	Path
ON	device.inp	#lcharge	device/Charge on left contact
ON	dos0.inp	#mueffe	dos0/Electron mobility
OFF	dos0.inp	#mueffh	epitaxy/MAPbI3/dos/Hole mobility
OFF	dos0.inp	#Etrape	dos0/Electron tail slope
OFF	dos0.inp	#ion_density	epitaxy/MAPbI3/dos/Perovskite ion density
OFF	dos0.inp	#srhsigmap_e	dos0/Trapped electron to Free hole
OFF	dos0.inp	#Ntrape	dos0/Electron trap density
ON	parasitic.inp	#Rcontact	parasitic/Series resistance
OFF	dos0.inp	#srhsigman_e	dos0/Free electron to Trapped electron
ON	parasitic.inp	#Rshunt	parasitic/Shunt resistance
OFF	light.inp	#Dphotoneff	light/Photon efficiency
OFF	dos0.inp	#srhsigman_h	dos0/Trapped hole to Free electron
OFF	dos0.inp	#srhsigmap_h	dos0/Free hole to Trapped hole
ON	dos0.inp	#free_to_free_recombination	o/dos/n_{free} to p_{free} Recombination rate constant

Figure A.3: Process for using "Fit to Experimental Data" function on GPVDM software. a) An example of imported experimental data. b) An image of the fit configure window which allows for different parameters to be varied or fixed. c) An image of the "Run Fit" program which attempts to fit the experimental data as accurately as possible [45].

B Ways to Test for Thermoreflectance Heating

We believe that the amplitude images coming from our thermoreflectance images might show the entire OPV cell have an increased change in reflectivity in addition to the hot spot. The following appendix are possible test to prove this hypothesis.

A. Thermoelectric Cooler

One way to test the heating hypothesis by using a thermoelectric cooler (TEC) to modulate the temperature of the unbiased cell while measuring the resulting thermoreflectance signal. A TEC is a multifaceted temperature device because it does not have moving parts and can be used for both heating and cooling be reversing its current flow [46]. A TEC is typically made of some ceramic material where one side allows for heat to be absorbed and the other allows for it to be dissipated. There are four physical phenomena that happen within a TEC, the Seebeck effect, the Peltier effect, the Thomson effect, and the Joule effect. The Seebeck effect occurs when a temperature change is sustained on the two sides of the TEC, generating voltage. The Peltier effect occurs when an electrical current is passed between two dissimilar junctions, allowing for a either a heating or cooling effect. The Thomson effect occurs when an electrical current is passed in the direction of a temperature gradient, allowing for either a heating or cooling effect in a homogeneous conductor. Finally, the Joule effect occurs when an electrical current is passed through a conductor, allowing for a heating effect in the conductor. We can potentially use a TEC to heat an OPV cell and measure the temperature of different parts of the cell in order to confirm that as the cell is biased, both it and its hotspot is increasing with heat.

B. Imaging OPV Device in Reverse

Another option is to compare our initial results obtained by imaging the light-absorbing side of the cell to imaging of the back-side silver (Ag) contact. Fig. 4.2 shows how our OPV devices are made inverted, with light being absorbed through the transparent substrate (glass) and cathode (ITO). We typically image the cell in this configuration; however, we are concerned that there are too many layers between the initial entrance of the LED light, and the Ag anode which we are using as our point of reflection in our thermoreflectance imaging technique. We can potentially image from the back, Ag contact, to see if we can avoid having the entire cell heat when using the technique.

C. Biasing OPV Device with Current

a. Howland Current Source

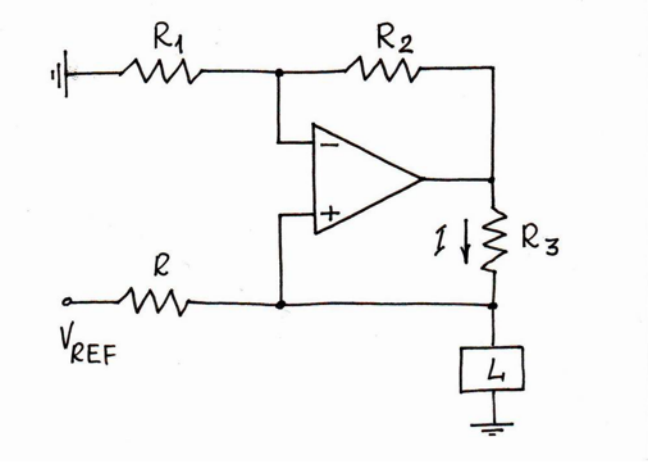

Figure B.1: Diagram of a typical Howland Current Source [47].

Fig. B.1 is a diagram of a Howland Current Source (HCS) looks like. R_1, R_2, R_3 and R are all resistors, I is current, V_{REF} is the reference voltage, and L is some load. We test the HCS with three different loads: a resistor, a diode, and finally an OPV. We test the HCS with three different loads: a resistor, a diode, and finally an OPV. When taking data for the resistors, we use different sizes in order to see what range the source worked with (between 20k and 90k). With each resistor, we use a function generator connected to our HCS and, using an oscilloscope, we look at the graph of function generator output voltage to what the voltage is after going through the HCS, ranging from 500mV to 1V. We receive the correct current range that we are looking for (10-4 Amps). When trying to do this with a diode however, we notice the top and bottom of the graph on the oscilloscope cut-off. In addition, at such low currents, at low currents the measurements seen from the oscilloscope are very off from the ones that we measure. There could have been a lot of potential problems, such as the resistors in the HCS being too small or large, that we did not really look into. Instead of looking into, for time-sake, we decide to try another method.

b. Conventional Transistor

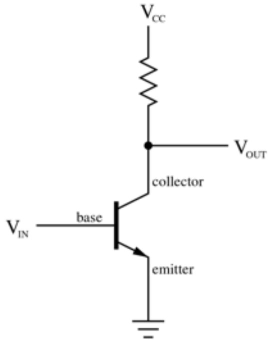

Figure B.2: Diagram of a typical transistor [47].

Fig. B.2 is a diagram of a typical transistor. V_{IN} is the voltage in, V_{CC} is the DC voltage supplied to the collector, and V_{OUT} is the voltage out. Fixing V_{CC} and V_{IN}, we want to see if we would get the proper output voltage that we are expecting. Once again, we start off by testing a few resistors (similar to the range from the HCS loads). The measured calculations that we find are very similar to that we calculated. We then move on to test a diode. In order to properly use the transistor as a way to step down the current for a diode, we first take IV curves of a typical diode. We want to use make sure that the current we are biasing the diode with is within the turn-on voltage range for a diode. When taking data for the diode, we find that our measurements are all slightly off from our calculated measurements. Due to time, we decide to hold off on completing this test.

c. Conventional Attenuator

An attenuator is a device that reduces the strength of a signal. We quickly test two different attenuators (at 3 and 6 dB) and see with the oscilloscope that the voltage the function generator output was stepping down properly. Once again due to time, we also decide to hold off on completing this test.

D. Conclusion

As said earlier, the ultimate goal was to determine the reasoning for the whole-cell heating. Above are some options on how to test this. Once we have confirmed whole-cell heating, the next step would be to find new defects in new OPV device and compare this new data with previous data and conventional methods of imaging.

C Bibliography

[1] F. Manzano-Agugliaro, A. Alcayde, et. al, “Scientific Production of Renewable Energies Worldwide: An Overview,” *Renewable and Sustainable Energy Reviews*, Vol. 18, 6 November 2012, pp. 134-143. Scientific Production of Renewable Energies Worldwide: An Overview.

[2] Unknown, “Energy and the Environment Explained,” *U.S. Energy Information Administration*, 19 June 2019. Energy and the Environment Explained.

[3] Unknown, “Nuclear Power in the World Today,” *World Nuclear Association*, January 2020. Nuclear Power in the World Today.

[4] Unknown, “Renewable Energy Explained,” *U.S. Energy Information Administration*, 2018. Renewable Energy Explained.

[5] L. M. Fraas, “Low-Cost Solar Electric Power,” *Springer International*, 2014, pp. 1-11. Low-Cost Solar Electric Power.

[6] Unknown, “Best Research-Cell Efficiency Chart,” *National Renewable Energy Laboratories*. Best Research-Cell Efficiency Chart.

[7] Unknown, “Perovskites and Perovskite Solar Cells: An Introduction,” *Ossila*. Perovskites and Perovskite Solar Cells: An Introduction.

[8] M.A. Green, “The Path to 25% Silicon Solar Cell Efficiency: History of Silicon Cell Evolution,” *Wiley Interscience*, Vol. 17, 25 March 2009, pp. 183-189. The Path to 25% Silicon Solar Cell Efficiency: History of Silicon Cell Evolution.

[9] M. Jacoby, “The Future of Low-Cost Solar Cells,” *Chemical and Engineering News*, Vol. 94: 18, 2 May 2016, pp. 30-35. The Future of Low-Cost Solar Cells.

[10] H. Tang, S. He, C. Peng, “A Short Progress Report on High-Efficiency Perovskite Solar Cells,” *Nanoscale Research Letters*, 2017, Vol. 12: 410, 14 June 2017. A Short Progress Report on High-Efficiency Perovskite Solar Cells.

[11] J. Bredas, J.R. Durrant, “Organic Photovoltaics,” *Accounts of Chemical Research*, Vol. 42:11,

November 2009, pp. 1689-1690. Organic Photovoltaics.

[12] L. Meng, Y. Zhang, et. al, “Organic and Solution-Processed Tandem Solar Cells with 17.3% Efficiency,” *Science*, Vo. 361:6407, 14 September 2008, pp. 1094-1098. Organic and Solution-Processed Tandem Solar Cells with 17.3% Efficiency.

[13] J. Yu, Y. Zheng, J. Huang, “Towards High Performance Organic Photovoltaic Cells: A Review of Recent Development in Organic Photovoltaics,” *Polymers*, Vol. 6:9, 25 September 2014, pp. 2473-2509. Towards High Performance Organic Photovoltaic Cells: A Review of Recent Development in Organic Photovoltaics.

[14] J. Bisquert, “The Physics of Solar Cells,” *Taylor Francis Group*, 2018. The Physics of Solar Cells.

[15] M. Poblocki, “Photoelectric Effect,” *Physics Experiments*, 2014. Photoelectric Effect.

[16] W.D. Callister, D.G. Rethwisch, “Materials Science and Engineering: An Introduction,” *John Wiley Sons Inc.*, 2014.

[17] Unknown, “Schottky Diode,” *Physics and Radio Electronics*. Schottky Diode.

[18] Unknown, “Simulation of an Organic Photovoltaic Cell (OPC) Using ATLAS,” *Simulation Standard*, August 2007. Simulation of an Organic Photovoltaic Cell (OPC) Using ATLAS.

[19] M.A. Green, “Photovoltaic Principles,” *Physica E: Low-dimensional Systems and Nanostructures*, Vol. 14:1-2, April 2002, pp. 11-17. Photovoltaic Principles.

[20] Y. Xu, T. Gong, J.N. Munday, “The Generalized Shockley-Queisser Limit for Nanostructured Solar Cells,” *Scientific Reports*, Vol. 5:13536. The Generalized Shockley-Queisser Limit for Nanostructured Solar Cells.

[21] C. Honsberg, S. Bowden, “PV Education,” *PV Education.org*, 2019. PV Education.

[22] L.W. Veldhuizen, C.H.M. van der Werf, et. al, “Optimization of Hydrogenated Amorphous Silicon Germanium Thin Films and Solar Cells Deposited by Hot Wire Chemical Vapor Deposition,” *Thin Solid Forms*, Vol. 13, May 2015, pp. 226-230. Optimization of Hydrogenated Amorphous Silicon Germanium Thin Films and Solar Cells Deposited by Hot Wire Chemical Vapor Deposition.

[23] M.A. Green, E.D. Dunlop, "Solar Cell Efficiency Tables (Version 54)," *Progress in Photovoltaics*, Vol. 27, 20 June 2019, pp. 565-575. Solar Cell Efficiency Tables (Version 54).

[24] H. Maghsoudi, "Short Overview of Perovskite Solar Cells," *SlideShare*, 27 February 2015. Short Overview of Perovskite Solar Cells.

[25] K. Popov, "Band Gap Engineering of Hybrid Organic Inorganic Lead-Halide Perovskites," *SlideShare*, 6 November 2014. Band Gap Engineering of Hybrid Organic Inorganic Lead-Halide Perovskites.

[26] A.Suzuki, H. Okada, and T. Oku, "Fabrication and Characterization of CH3NH3PbI3-x-yBrxCly Perovskite Solar Cells," *Energies*, Vol. 9:376, May 2016. Fabrication and Characterization of CH3NH3PbI3-x-yBrxCly Perovskite Solar Cells.

[27] D. Huang, A. D. Taylor, et. al, "Perovskite Solar Cells with a DMSO-Treated PEDOT:PSS Hole Transport Layer Exhibit Higher Photovoltaic Performance and Enhanced Durability," *Nanoscale*, Vol. 9, 23 February 2017, pp. 4236-4243. Perovskite Solar Cells with a DMSO-Treated PEDOT:PSS Hole Transport Layer Exhibit Higher Photovoltaic Performance and Enhanced Durability.

[28] M. Li, Z-K Wang, et. al, "Copper Salts Doped Spiro-OMeTAD for High-Performance Perovskite Solar Cells," *Advanced Energy Materials*, Vol. 6:21, 6 August 2016. Copper Salts Doped Spiro-OMeTAD for High-Performance Perovskite Solar Cells.

[29] Unknown, "LiTFSI," *Ossila*. LiTFSI.

[30] J.A. Rohr, J. Nelson, et. al, "Charge Transport in Spiro-OMeTAD Investigated through Space-Charge-Limited Current Measurements," *Physical Review Applied*, Vol. 9:4, 12 April 2018. Charge Transport in Spiro-OMeTAD Investigated through Space-Charge-Limited Current Measurements.

[31] S.E. Shaheen, C.J. Brabec, N.S. Sariciftci, "2.5% Efficient Organic Plastic Solar Cells," *Applied Physics Letters*, Vol. 78:6, 2 February 2001, pp. 841-843. 2.5% Efficient Organic Plastic Solar Cells.

[32] F.C. Krebs, "Polymeric Solar Cells: Materials, Design, Manufacture," *DEStech Publications Inc.*, 2010.

[33] C. Duan, C. Zhong, et. al, "Interface Engineering for High Performance Bulk-Heterojunction Polymeric Solar Cells," *Organic Solar Cells*, Springer, 2013, pp. 43-79. Interface Engineering for

High Performance Bulk-Heterojunction Polymeric Solar Cells.

[34] A. Polman, M. Knight, “Photovoltaic Materials: Present Efficiencies and Future Challenges,” *Science*, Vol. 352:6283, 15 April 2016. Photovoltaic Materials: Present Efficiencies and Future Challenges.

[35] O. Breitenstein, J.P. Rakotoniaina, “Shunt Types in Crystalline Silicon Solar Cells,” *Progress in Photovoltaics*, Vol. 12, 29 July 2004, pp. 529-538. Shunt Types in Crystalline Silicon Solar Cells.

[36] M. Kasemann, D. Grote, “Shunt Detection Capabilities of Luminescence Imaging on Si Solar Cells,” *Presented at the 22nd European Photovoltaic Solar Energy Conference and Exhibition*, 3 - 7 September 2007, Milan, Italy. Shunt Detection Capabilities of Luminescence Imaging on Si Solar Cells.

[37] O. Breitenstein, J. Bauer, et. al, “Can Luminescence Imaging Replace Lock-in Thermography on Solar Cells?,” *IEEE Journal of Photovoltaics*, Vol. 1:2, 17 October 2011, pp. 159-167. Can Luminescence Imaging Replace Lock-in Thermography on Solar Cells?.

[38] M. Kasemann, D. Grote, et. al, “Luminescence Imaging for the Detection of Shunts on Silicon Solar Cells,” *Progress in Photovoltaics*, Vol. 16, 22 January 2008, pp. 297-305. Luminescence Imaging for the Detection of Shunts on Silicon Solar Cells.

[39] O. Breitenstein, J.P. Rakotoniaina, M.H. Al Rifai, “Quantitative Evaluation of Shunts in Solar Cells by Lock-In Thermography,” *Progress in Photovoltaics*, Vol. 11, 5 December 2003, pp. 515-526. Quantitative Evaluation of Shunts in Solar Cells by Lock-In Thermography.

[40] Q. Zhou, J. Hudgings, et. al, “High Spatial Resolution Characterization of Silicon Solar Cells Using Thermoreflectance Imaging,” *Journal of Applied Physics*, Vol. 110:5, 15 September 2011, pp.153-161. High Spatial Resolution Characterization of Silicon Solar Cells Using Thermoreflectance Imaging.

[41] D.L. Decker, V.A. Hodgkin, “Wavelength Temperature Dependence of the Absolute Reflectance of Metals at Visible and Infrared Wavelengths,” *Laser Induced Damage in Optical Material*, 1980, pp. 190-200.

[42] K. Allison, “Thermoreectance Imaging: Noise Analysis,New Algorithms, and Stochastic Reso-

nance," *Pomona College Physics Department*, 18 April 2018.

[43] T. Jones, "Defect Characterization of Organic Photovoltaic Cells," *Pomona College Physics Department*, 19 April 2018.

[44] R. Mackenzie, "GPVDM", *GPVDM*. GPVDM.

[45] R. Mackenzie, "Extracting Mobility and Recombination Rates From Experimental Data Using GPVDM," *GPVDM*, *YouTube*, 20 April 2019. Extracting Mobility and Recombination Rates From Experimental Data Using GPVDM.

[46] J.A. Chavez, J.A. Ortega, et. al, "SPICE Model of Thermoelectric Elements Including Thermal Effects," Proceedings of the 17th IEEE Instrumentation and Measurement Technology Conference, Vol. 2, 2000, Baltimore, MD, USA, pp. 1019-1023. SPICE Model of Thermoelectric Elements Including Thermal Effects.

[47] P. Horowitz, W. Hill, "The Art of Electronics," *Cambridge University Press*, 2015.